


 Cite this: *Lab Chip*, 2021, 21, 2511

Direct isolation of circulating extracellular vesicles from blood for vascular risk profiling in type 2 diabetes mellitus†

 Hui Min Tay,^a Sheng Yuan Leong,^a Xiaohan Xu,^a Fang Kong,^b Megha Upadya,^b Rinkoo Dalan,^{cd} Chor Yong Tay,^e Ming Dao,^{bf} Subra Suresh^{*e} and Han Wei Hou^{id*ad}

Extracellular vesicles (EVs) are key mediators of communication among cells, and clinical utilities of EVs-based biomarkers remain limited due to difficulties in isolating EVs from whole blood reliably. We report a novel inertial-based microfluidic platform for direct isolation of nanoscale EVs (exosomes, 50 to 200 nm) and medium-sized EVs (microvesicles, 200 nm to 1 μm) from blood with high efficiency (three-fold increase in EV yield compared to ultracentrifugation). In a pilot clinical study of healthy ($n = 5$) and type 2 diabetes mellitus (T2DM, $n = 9$) subjects, we detected higher EV levels in T2DM patients ($P < 0.05$), and identified a subset of “high-risk” T2DM subjects with abnormally high (~10-fold to 50-fold) amounts of platelet (CD41a+) or leukocyte-derived (CD45+) EVs. Our *in vitro* endothelial cell assay further revealed that EVs from “high-risk” T2DM subjects induced significantly higher vascular inflammation (ICAM-1 expression) ($P < 0.05$) as compared to healthy and non-“high-risk” T2DM subjects, reflecting a pro-inflammatory phenotype. Overall, the EV isolation tool is scalable, and requires less manual labour, cost and processing time. This enables further development of EV-based diagnostics, whereby a combined immunological and functional phenotyping strategy can potentially be used for rapid vascular risk stratification in T2DM.

 Received 16th April 2021,
 Accepted 23rd May 2021

DOI: 10.1039/d1lc00333j

rsc.li/loc

Introduction

Extracellular vesicles (EVs) are membrane-bound vehicles secreted by cells and they contain different types of cargo such as lipids, nucleic acids and proteins.¹ They are key mediators of intercellular communication, and are implicated in many biological processes and diseases.^{2,3} While the definition and nomenclature of EVs subtypes are constantly evolving,^{4,5} EVs are commonly categorized into three main groups depending on their size and biogenesis: (1) apoptotic bodies (>1000 nm in size) derived from apoptotic cells, (2) microvesicles (~200 to 1000 nm in diameter) shed from

plasma membrane, and (3) nanoscale exosomes (~50 to 200 nm in diameter) secreted from endosomal pathways.⁶ EVs circulating in whole blood form a new class of biomarkers^{7–9} in liquid biopsy as they are highly stable, abundant (~10^{11–12} per mL of blood),¹⁰ and may contain functional or disease-specific proteins or microRNA for disease diagnostics.¹¹

Type 2 diabetes mellitus (T2DM) is a chronic metabolic disease characterized by hyperglycemia and low-grade inflammation in blood. The major cause of mortality and morbidity in T2DM arises from micro- and macro-vascular complications.¹² A serious consequence of such complications is that T2DM patients are at two to four times higher risk of developing cardiovascular diseases (CVD) compared to non-diabetics.¹³ Circulating microvesicles (or microparticles) are widely studied in CVD and T2DM as mediators of endothelial activation and dysfunction.^{14–17} Exosomes from diabetic patients are also considered to modulate endothelial and immune functions.^{18,19} However, the clinical utilities of blood-borne EVs remain poorly explored due to the lack of standardization in EVs sample preparation, and the limited means available today to extract nanoscale exosomes in sufficient quantities from complex biofluids such as whole blood.

Currently techniques for EVs isolation involve differential ultracentrifugation (UC) and density gradient UC which

^a School of Mechanical and Aerospace Engineering, Nanyang Technological University, 50 Nanyang Avenue, Block N3, 639798, Singapore.

E-mail: hwhou@ntu.edu.sg

^b School of Biological Sciences, Nanyang Technological University, 60 Nanyang Drive, 637551, Singapore

^c Endocrine and Diabetes, Tan Tock Seng Hospital, 11 Jalan Tan Tock Seng, 308433, Singapore

^d Lee Kong Chian School of Medicine, Nanyang Technological University, 11 Mandalay Road, Clinical Sciences Building, 308232, Singapore

^e School of Material Science and Engineering, Nanyang Technological University, 50 Nanyang Avenue, Block N4.1, 639798, Singapore. E-mail: ssuresh@ntu.edu.sg

^f Department of Material Science and Engineering, Massachusetts Institute of Technology, 182 Memorial Dr, Cambridge, MA 02142, USA

† Electronic supplementary information (ESI) available. See DOI: 10.1039/d1lc00333j

isolate EVs by size and density at high centrifugation speeds ($\sim 200\,000$ rpm) in a batch processing mode. However, UC is laborious, time-consuming (up to 5–6 h to complete) and suffers from low EVs yield (~ 5 to 10%).⁶ Other commercial EV isolation methods such as polymer-based precipitation,⁸ tangential flow filtration (TFF),²⁰ and asymmetrical flow field fractionation (AF4)^{5,21} can improve EV yield and/or reduce protein contamination, but are generally limited by their low throughput and scalability. Size-exclusion chromatography (SEC) is increasingly used for EV isolation,^{22,23} and can achieve high sample throughput by using larger SEC columns. However, it cannot process whole blood directly (requires plasma as the starting sample) and involves numerous manual handling steps during operation (buffer addition, collection of eluted EV fractions *etc.*). Microfluidic technologies are attractive alternatives for isolation of EVs due to their miniaturized footprint and high potential for automation and point-of-care applications. Passive microfluidic EVs isolation methods include membrane nanofiltration,^{9,24} deterministic lateral displacement (DLD) in a nano-pillar array,²⁵ and size-dependent viscoelastic particle focusing.²⁶ Active microfluidic EVs sorting use acoustic separation,^{27,28} or employ electrical forces²⁹ or immuno-affinity EVs capture^{30,31} to isolate and detect exosomes directly from plasma. However, these platforms often entail complicated steps in fabrication and operation, and they lack speed, reproducibility, and economies of scale in large-scale clinical testing. Recent advances in spiral inertial microfluidics technology, termed Dean flow fractionation (DFF), enables high throughput sorting of cells (~ 10 to $20\ \mu\text{m}$ in diameter),^{32,33} and this method can be further exploited for separation³⁴ of small particles (~ 1 to $3\ \mu\text{m}$ in diameter). However, separation of nano-sized particles ($< 1\ \mu\text{m}$) is still considered impractical in conventional inertial microfluidics devices as the size-dependent inertial forces are negligible for equilibrium focusing of particles.³⁵ Hence, there exists a critical need to develop novel methods to isolate EVs which are economical, high-throughput, simple to use, and readily adaptable in clinical settings.

Here, we report the development of a microfluidics device (ExoDFF) for direct isolation of circulating EVs from whole blood (1:1 dilution). Unlike conventional inertial microfluidics devices which achieve size-dependent focusing of large particles (~ 5 to $30\ \mu\text{m}$) based on the balance of inertial lift and Dean drag forces,^{36–38} our technology utilizes differential Dean-induced lateral migration of small particles (transient effect) to achieve separation. This label-free approach enables simultaneous sorting of nanoscale and medium-sized EVs into different device outlets to facilitate downstream characterization (Fig. 1A and S1†). We first demonstrated the performance characteristics and advantages of ExoDFF with higher eluted concentration and yield of EVs (both approximately three-fold) when compared to standard UC methods. We next applied this microfluidic device as a possible whole-blood-based diagnostic tool to assess vascular risk in T2DM patients. As a proof-of-concept,

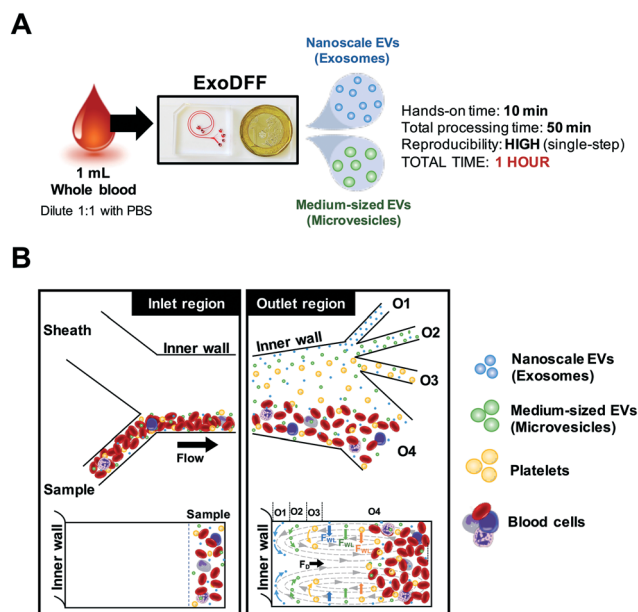


Fig. 1 Microfluidic isolation of EVs using ExoDFF. (A) Schematic workflow of ExoDFF device for isolation of circulating EVs from diluted whole blood (1:1). Photograph shows the spiral device filled with red dye for visualization. Figure made with BioRender. (B) Schematic illustration of ExoDFF separation principle. Under the influence of Dean vortices in spiral microchannels, EVs and platelets (particle size (a_p)/hydraulic diameter (D_h) < 0.07) migrate laterally toward the channel inner wall while larger blood cells (~ 6 to $15\ \mu\text{m}$) remain close to the outer wall. Near the inner wall, smaller particles occupy subtle differences in innermost transient positions due to size-dependent wall-induced inertial lift forces (F_{WL}), which result in nanoscale EVs (exosomes, ~ 50 to $200\ \text{nm}$) and medium-sized EVs (microvesicles, $\sim 200\ \text{nm}$ to $1000\ \text{nm}$) sorted into O1 (ExoDFF NV) and O2 (ExoDFF MV), respectively.

we isolated EVs from healthy individuals ($n = 5$) and T2DM subjects ($n = 9$). Through immunophenotyping of ExoDFF EVs, we identified a subset of “high-risk” T2DM subjects with abnormally high (~ 10 to 50-fold) levels of platelet (CD41a+) or leukocyte-derived (CD45+) EVs when compared to the average values for healthy subjects. *In vitro* endothelial cell assays further revealed that EVs from “high-risk” T2DM subjects induced the highest vascular inflammation (ICAM-1 expression) as compared to healthy and non “high-risk” T2DM EVs, thus reflecting a pro-inflammatory phenotype. Comparative studies of different EVs isolation methods also indicated a significant increase in EV-induced ICAM-1 expression using UC *versus* ExoDFF and SEC, which points to the importance of gentle sorting of EVs to assess their functionality. To further enhance the translational utility, we have developed a multiplexed high throughput ExoDFF (ExoDFF^{HT}) device that is capable of processing 5 mL of whole blood within an hour. These findings presented here suggest new possibilities for the development of a single-step and scalable immunophenotyping method whereby rapid purification of blood-borne EVs can be achieved. This technique also serves as a unique blood-based, liquid biopsy testing strategy for vascular risk stratification in T2DM predicated on vascular inflammation induced by EVs.

Experimental section

Device operation

For the characterization of beads that served as proxy for particles, bead samples and sheath buffer (phosphate buffered saline (PBS; Lonza, Basel, Switzerland)) were perfused into the device using separate syringe pumps (CX Fusion 200, Chemyx Inc., Stafford, TX, USA). The setup was allowed to run for 5 min to stabilize the flow before collecting the eluents from the outlets. The device was mounted on a Nikon Eclipse Ti inverted phase-contrast microscope (Nikon Instruments Inc., Melville, NY, USA) equipped with Metamorph software (WSN-META-MMACQMIC, Molecular Devices, Sunnyvale, CA, USA) for visualizing bead equilibrium flow positions based on fluorescence imaging. For blood processing, the blood sample (diluted 1:1 with PBS) and sheath buffer were perfused into the sample inlet at optimized flow rates of 40 $\mu\text{L min}^{-1}$ and 400 $\mu\text{L min}^{-1}$ respectively (1:10). Outlet eluents were collected after the flow had stabilized and phase-contrast high-speed videos (10 000 fps) were captured using a Phantom V9.1 high-speed camera (Vision Research, Wayne, NJ, USA).

Ultracentrifugation (UC)

Circulating blood EVs were isolated using an ultracentrifuge (Optima XE-90, Beckman Coulter, Brea, CA, USA), equipped with a SW41Ti rotor. Briefly, blood sample were first centrifuged at $2500 \times g$ for 15 min to remove blood cells and platelets. The platelet-poor plasma (PPP) was then transferred to a UC tube (Beckman Coulter) and filled to 11 mL with filtered PBS. To pellet microvesicles (UC MV), the sample was centrifuged at $20\,000 \times g$ for 60 min at 4 °C and re-suspended to 300 μL of PBS per 1 mL of whole blood. To pellet exosomes (UC Exo), the supernatant was filtered through a 0.22 μm filter prior to UC at $210\,000 \times g$ for 70 min at 4 °C, then re-suspended to 300 μL of PBS per 1 mL of whole blood.

Nanoparticle tracking analysis (NTA)

The size distribution and concentration of EVs were analysed using NTA with NanoSight system (NS300, Malvern Panalytical, Malvern, Worcestershire, UK) and Zetaview (PMX-120, Particle Metrix, Meerbusch, Germany). For both methods, samples were diluted to the recommended particle concentration per frame with filtered PBS prior analysis. For NanoSight, the video segments captured for each measurement were analysed by NanoSight Software NTA 3.1 (Malvern Panalytical). For Zetaview (Particle Metrix), particle motion was measured over 11 positions with two repeat measurements at each position. The following machine setting was applied: frame rate: 30 fps; number of frames recorded: 60; sensitivity: 80; exposure: 100; minimum brightness: 30; minimum pixel size: 10; maximum pixel size: 10000; trace length: 30; temperature: 25 °C. Measurement

results were exported in .txt format and corrected with dilution factor using MATLAB (MathWorks).

Flow cytometry analysis

Flow cytometry analysis was performed using a BD LSR flow cytometer (Fortessa X-20, BD Biosciences, San Jose, CA, USA). All antibodies were purchased from eBioscience (Thermo Scientific, MA, USA) and used for staining (1:20 dilution) at 4 °C for 30 min. Unstained samples and respective isotype antibodies were used as negative controls. For HUVEC inflammatory marker analysis, the cells were stained with PE-conjugated anti-human CD54 antibody (ICAM-1) and washed once after staining. For EVs immunophenotyping, UC isolated microvesicles (UC MV) and microvesicles from ExoDFF device outlet 2 (ExoDFF MV) samples were stained with FITC-conjugated anti-human CD41a antibody (platelet-derived microvesicles) and APC-conjugated anti-human CD45 antibody (leukocytes-derived microvesicles) and quenched with 5 volumes of PBS after staining. A fixed volume of 3 μm beads (of known concentration) was added to each sample prior flow cytometry analysis, and initial microvesicles concentration from blood was quantified based on the detection of ~2000 control beads.

Study approval

Written informed consent was obtained from all subjects during recruitment for this study. Healthy and T2DM subjects recruited for clinical comparison were of a fasting state for accurate measurements of preprandial blood glucose. Healthy volunteers recruited for supplemental experiments for comparison of isolation methods were of non-fasting state. Whole blood samples were collected from venipuncture into sodium citrate vacutainers (BD Biosciences), and protocols were approved by the institutional review boards (IRB) of Nanyang Technological University (IRB-2019-03-011) and Tan Tock Seng Hospital (DSRB 2018/00880).

Statistical analysis

All numerical data were expressed as the mean \pm s.e.m, unless otherwise specified. We assessed the statistical significance of the difference between two sets of data using the Mann-Whitney *U*-test (unless otherwise specified) with $P < 0.05$ considered to be of significant difference. Clinical samples with incomplete set of measurements for clinical comparison (NTA, flow cytometry, endothelial uptake assay) were excluded from analysis. All analysis was performed using GraphPad Prism V8.0 (GraphPad Software, San Diego, CA, USA).

Results

Microfluidic isolation of EVs using Dean flow fractionation

Inertial microfluidics is an area of research dealing with hydrodynamic manipulation of engineered particles and

biological entities of different shapes,^{39,40} dimensions³⁵ and mechanical properties.^{41,42} These platforms offer precise control of particle focusing by tuning channel geometries.^{43,44} They can also enhance separation resolution for label-free cell sorting applications^{33,45} through the introduction of secondary flows (e.g. Dean flow). In conventional inertial focusing devices, particles equilibrate at distinct flow positions due to the balance of inertial and Dean drag forces.^{36–38} We recently reported that small particles in DFF devices experience differential size-dependent wall-induced lift forces (F_{WL} , directed away from wall) as they migrate along the top and bottom of the channel due to counter-rotating Dean vortices.³⁴ Near the inner wall, they occupy different innermost distances (D_{inner}) due to subtle differences in their z -positions (orthogonal to the direction of particle flow) during lateral migration. Note that this phenomenon is transient (non-steady-state), and it operates at lower flow rate conditions (at Reynolds number, Re , between 20 and 50) where inertial focusing effects (that typically occur at $Re \sim 100$ to 200) are not yet established.^{36,37} Here, we apply the separation principle to develop a DFF-based fractionation tool (ExoDFF) for EVs by including a channel expansion region prior to the channel outlets, and optimizing the outlet elution volumes with non-uniform fluidic resistances. These enable us to achieve a higher separation resolution which can be exploited for simultaneous separation and enrichment of nanoscale EVs (exosomes, ~ 50 to 200 nm in diameter) and medium-sized EVs (microvesicles, ~ 200 nm to 1 μm in diameter) from diluted whole blood (1 : 1). The 2-inlet, 4-outlet ExoDFF device is 300 μm in width (w) \times 55

μm in height (h) with a radius of ~ 0.5 to 0.6 cm. Diluted blood sample is introduced at channel outer wall, where smaller blood components (platelets and EV, particle size (a_p)/hydraulic diameter (D_h) < 0.07) migrate laterally toward the inner wall under the influence of Dean vortices. Near the inner wall, they occupy different D_{inner} , which leads to continuous fractionation of nanoscale EVs into outlet 1 (ExoDFF NV, O1), medium-sized EVs into outlet 2 (ExoDFF MV, O2), and platelets (~ 2 to 3 μm) into outlet 3 (O3). Larger blood cells (~ 6 to 15 μm , RBCs and WBCs) experience significant Stoke's drag,⁴⁵ and remain closer to the outer wall for efficient removal *via* outlet 4 (O4) (Fig. 1B).

Numerical study of lateral migration of EVs

We first performed computational fluid dynamics (CFD) simulations to investigate the migration profile of EVs (Fig. 2). Fluid streamlines were used to represent trajectories as it is not practical to fully resolve EVs ($\sim 10^{-7}$ m) in microfluidic channels ($\sim 10^{-4}$ m). In addition, the deformation of flow field due to EVs is negligible,³⁶ and particle-particle interaction is minimal as the particles ($\sim 10^9$ – 10^{11} mL⁻¹) comprise less than 0.05% of the fluid by volume. As shown in Fig. 2A, fluid streamlines (green) were initiated from the sample inlet at the outer wall. Under the influence of Dean vortices, the streamlines migrated along the channel top and bottom toward the inner wall. Prior to the channel outlets, the streamlines reached the inner wall and migrated downward to the channel midline in the direction of Dean vortices. At the optimal flow rate ($Re \sim 40$),

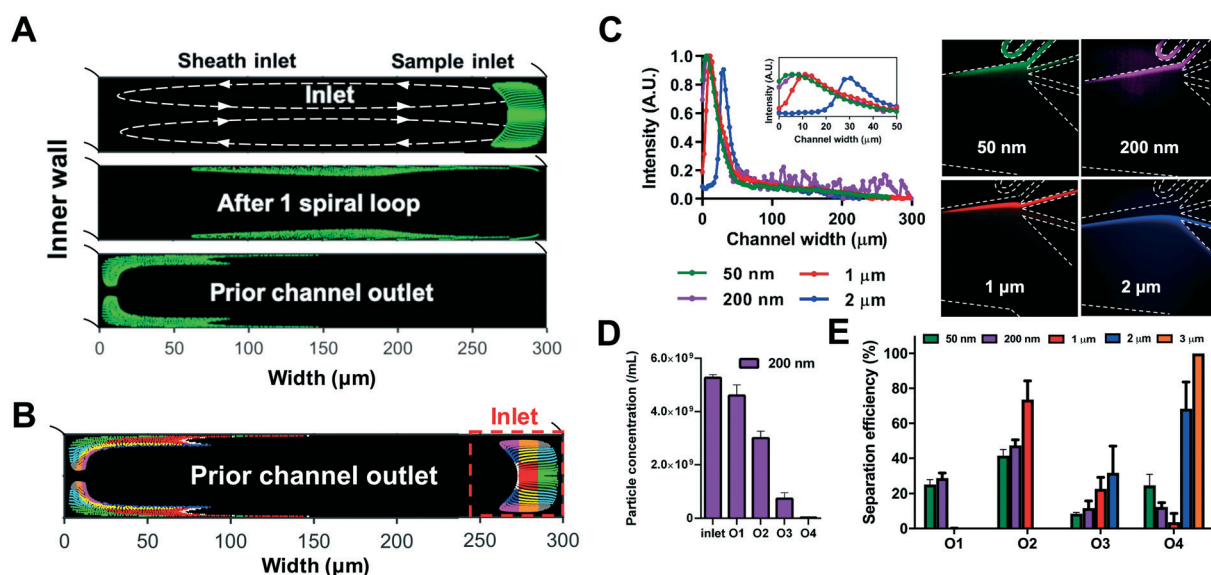


Fig. 2 Computational fluid dynamics simulation and bead characterization. (A) Cross sectional views of green fluid streamlines (mimicking flow of EVs) at different channel positions using CFD. Streamlines initiated from sample inlet (pinched to outer wall at sample to sheath flow rate ratio of 1 : 20 ($\sim 23 \mu\text{L min}^{-1}$: $\sim 457 \mu\text{L min}^{-1}$)) migrate across the channel width along the channel top and bottom due to counter rotating Dean vortices towards the inner wall. (B) Composite cross-sectional view of channel outlet and inlet (red dashed box) with colour coded streamlines based on different initial positions at the inlet. (C) Average fluorescent intensity line scans indicating the flow position of 50 nm, 200 nm, 1 μm and 2 μm beads across the channel width at optimal flow condition ($Re = 40$). Corresponding fluorescent images illustrating bead flow streamlines and their separation into different outlets. (D) Particle concentration of 200 nm beads at the inlet and at different ExoDFF outlets based on nanoparticle tracking analysis (NTA) ($n = 3$). (E) Bead separation efficiency in each outlet based on NTA and flow cytometry ($n = 3$).

the streamlines were mostly located within 50 μm from the inner wall with a sample-to-sheath inlet flow rate ratio of 1:20. These CFD results were in good agreement with our experimental characterization of Dean migration profile for 50 nm beads (Fig. S2A–C†). This validation of our CFD model predictions motivated our design criterion for outlet 1 (ExoDFF NV), and the elution of fluid streamlines between 50 to 100 μm into outlet 2 (ExoDFF MV). We next studied different sample-to-sheath flow rate ratios and observed that the streamline distribution remained tightest at higher sample pinching ratios (1:40 to 1:10) (Fig. S3†). For better visualization, fluid streamlines were colour-coded based on their initial inlet positions. It was evident that the streamline trajectory was strongly dependent on the initial distance from the outer wall (Fig. 2B). Taken together, increased sample pinching at channel inlet (higher sample-sheath flow rate ratio) is beneficial for ExoDFF as it reduces the streamline distances from outer wall at the inlet, which leads to a tighter streamline distribution during lateral migration.

Experimental validation of microparticle separation

We further characterized different flow rates ($Re \sim 3$ to 60) and resultant particle migration (50 nm to 2 μm) induced by Dean drag forces using fluorescence imaging (Fig. 2C and S2D†). These bead sizes were chosen to represent the EV size range based on our definition, with 50 nm and 200 nm beads representing nanoscale EVs (50–200 nm in diameter) and 1000 nm beads representing medium-sized EVs (200–1000 nm in diameter). As expected, these small particles ($a_p/D_h < 0.07$) migrated completely toward the inner wall at $Re \sim 40$ as they were solely affected by the Dean drag forces. The focusing bands of 50 nm and 200 nm particles were very close (within a distance of 10 μm) to the inner wall which corroborated our CFD results (Fig. 2C). By contrast, focusing bands of 1 μm and 2 μm beads peaked at 10 μm and 30 μm from inner wall, respectively, and were clearly distinct from the 50 nm and 200 nm beads. To evaluate particle separation efficiency in our device, we used NTA for quantify 200 nm beads and flow cytometry for quantification of 1 to 3 μm beads to determine different bead outlet concentrations.

Separation efficiency was quantified based on the number of beads collected from a specific outlet divided by the sum of beads collected from all outlets. The concentration of 200 nm beads was the highest in O1 (ExoDFF NV) which was similar to inlet concentration despite a 1:20 sheath fluid dilution on-chip (Fig. 2D, Table S1†). Separation efficiencies of 50 and 200 nm beads in O1 (ExoDFF NV) were ~ 20 to 25% in O1 with no contamination of 1 μm and 2 μm beads (Fig. 2E). It should be noted that an overall higher separation efficiency of 200 nm was observed in O2 (ExoDFF MV) as the eluted flow rate was higher ($\sim 7 \mu\text{L min}^{-1}$ in O1 vs. $\sim 16 \mu\text{L min}^{-1}$ in O2) due to non-uniform hydraulic channel resistance, which led to higher total number of beads eluted in O2 per unit time. Separation efficiency of 1 μm beads was $\sim 70\%$ at O2 (ExoDFF MV), while 2 and 3 μm beads were

mostly eluted into O3 and O4. Hence, the size cut-off for outlet 1 (ExoDFF NV) is determined to be 50 to 200 nm, while outlet 2 (ExoDFF MV) is ~ 200 nm to 1 μm . There were also negligible differences in separation performance when we varied sample-sheath flow rate ratio (1:20 and 1:10) (Fig. S4†). Overall, these results clearly demonstrate that the current technique could offer an efficient membrane-free tool to size fractionate microparticles of smaller size range (~ 200 nm to 3 μm) which is not achievable in conventional inertial microfluidic devices (used for sorting ~ 5 to 20 μm diameter cells or particles).^{35,45}

Isolation of circulating EVs from diluted whole blood

Conventional UC based on differential and density gradients suffers from poor yield of EVs and reproducibility.⁶ Most isolation methods also require blood pre-processing (centrifugation) as they begin with platelet-poor plasma (PPP) as their starting sample.⁴⁶ To ensure minimal sample preparation in the ExoDFF process, diluted whole blood (1:1 PBS) and sheath fluid were perfused into the device at an optimized flow rate ($Re \sim 40$) of 40 $\mu\text{L min}^{-1}$ (sample) and 400 $\mu\text{L min}^{-1}$ (sheath). As shown by the high-speed images in Fig. 3A, larger blood cells (~ 6 to 15 μm) remained close to the channel outer wall before reaching outlets and were efficiently removed *via* waste outlet (O4). Smaller platelets (~ 2 to 3 μm) migrated further toward the inner wall and were sorted into both waste outlets (O3 and O4). We next collected the eluents from O1 and O2 (ExoDFF NV and MV, respectively) for downstream characterization of size distribution and particle yield using nanoparticle tracking analysis (NTA). Results were also compared with multi-step UC which is a widely used EVs isolation method. Both nanoscale EVs from ExoDFF and UC (see Experimental section) exhibited similar size distribution with a dominant peak at ~ 150 nm (Fig. 3B). By contrast, microvesicles isolated using ExoDFF and UC had a wider size distribution (~ 100 to 800 nm). It should be noted that the size distribution plots were generated by different dilution factors for ExoDFF NV and UC Exo, as the ExoDFF NV sample was $\sim 100\times$ more concentrated ($\sim 10^{11} \text{ mL}^{-1}$). The concentration of nanovesicles (NV) was the highest for ExoDFF (Fig. 3C), which translated to a separation efficiency of ~ 15 ($\pm 3.8\%$), and was about three times better than for UC (~ 4.8 ($\pm 4.2\%$)) (Fig. 3D). This also led to a significant improvement in EVs yield ($\sim 3\times$) ($P < 0.01$) (Fig. 3E), and thus suggests the ability of ExoDFF to isolate micro- and sub-micro-scale EVs in a single-step, as opposed to UC that is highly dependent on operator skills (more prone to EVs losses). Unlike 200 nm bead separation in PBS, the device waste outlet (O4) had the highest recovery ($\sim 50\%$) of EVs which could be attributed to the incomplete migration of EVs in a highly concentrated cellular background ($\sim 20\%$ hematocrit) (Fig. S5A†). While processing diluted blood samples can improve EV recovery (Fig. S5B and C†), the trade-off is longer processing time (lower throughput) and more diluted eluent of sorted EVs.

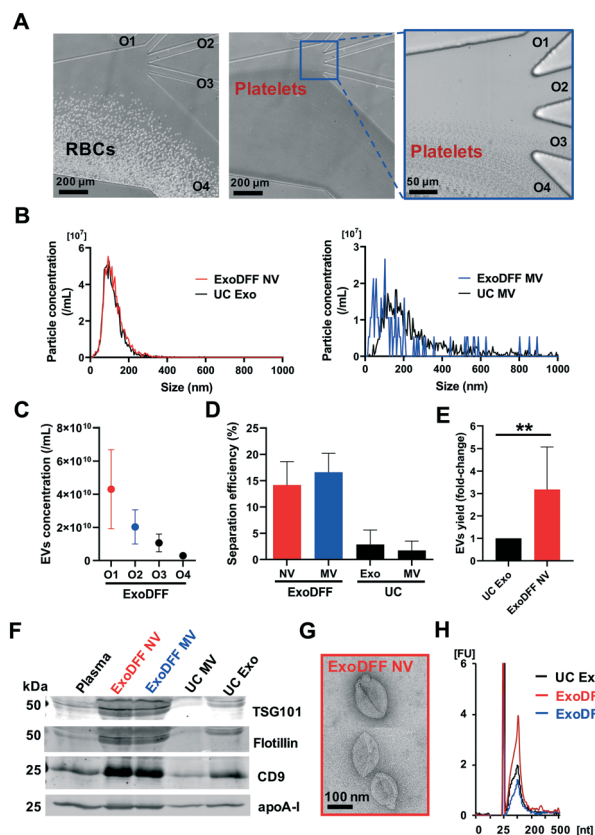


Fig. 3 Isolation of circulating EVs from whole blood (1:1). (A) High speed images illustrating separation of RBCs and platelets into O3 and O4 as waste. Inset (blue box) depicts platelet flow position. (B) Size distribution plots of ExoDFF NV ($1.0 \times 10^{11} \text{ mL}^{-1}$), UC exosomes ($9.2 \times 10^8 \text{ mL}^{-1}$), ExoDFF MV ($4.5 \times 10^8 \text{ mL}^{-1}$) and UC MV ($8.1 \times 10^7 \text{ mL}^{-1}$). Original particle concentrations are indicated in brackets. (C) EVs concentrations in different outlets of ExoDFF after separation ($n = 3$). (D) Comparison of EVs separation efficiencies between ExoDFF and UC ($n = 3$). (E) EVs yield comparison (fold-change) between UC Exo and ExoDFF NV ($n = 7$). $**p < 0.01$ based on unpaired Mann-Whitney test. (F) Western blot detection of exosomal markers TSG101, flotillin and CD9, and ApoA-1 for blood plasma. All samples were loaded with equal volume (15 μL) except plasma (0.5 μL). (G) TEM images of EVs with cup-shaped morphology isolated from ExoDFF NV. (H) MicroRNA analysis of EVs from ExoDFF and UC. Plot shows the size distribution in nucleotides and fluorescence intensity of total RNA. Peak at 25 nucleotides is an internal standard used as a lower marker in the RNA Pico assay. Data are presented as mean \pm s.d.

Hence, we propose that low blood dilution factors (1:1 to 1:2) will be more useful for ExoDFF testing in clinical settings to allow faster isolation and direct downstream analysis of enriched EVs. Similar EV separation performance was also observed with platelet-poor plasma (diluted 1:1 with PBS) which will be useful to process biobanked plasma samples retrospectively (Fig. S6[†]).

To validate the presence of EVs from ExoDFF and UC samples, exosomal protein markers TSG101, flotillin and CD9 were characterized using western blot. Consistent with NTA results, stronger signals were detected in ExoDFF as compared to UC with equal sample volumes, which qualitatively suggests higher EV concentrations after

processing (Fig. 3F and S5D[†]). As lipoproteins are major contaminants when EVs are isolated from plasma, the ApoA-I marker which indicates lipoprotein contamination, was detected in EVs isolated using ExoDFF and UC. Given the strong signal of protein markers in EVs, quantification of lipoprotein contamination could not be determined. Nevertheless, western blot results suggest that lipoprotein contamination in ExoDFF and UC were at similar levels.

Transmission electron microscopy (TEM) was also used to visualize EVs which revealed distinctive cup-shaped morphology of exosomes ~ 60 to 120 nm in size⁴⁷ (Fig. 3G). We also examined the total RNA content from EVs isolated using ExoDFF and UC, and examined RNA size distribution and yield using Bioanalyzer RNA Pico assay. Both ExoDFF and UC EVs showed short RNA profiles with a dominant peak below 200 nucleotides, which is representative of exosome-derived microRNA⁴⁸ (Fig. 3H). RNA yield from ExoDFF nanovesicles was the highest, which indicated high exosome concentration and corroborated both NTA and western blot results. As expected, ExoDFF waste outlets (O3 and O4) exhibited a wider size distribution with larger sized ribosomal RNA (rRNA) peaks due to the contamination of other blood cells (Fig. S5E[†]). Taken together, these results demonstrate that the present device offers efficient isolation of EVs. It can process diluted whole blood (1:1), and offers superior yield, shorter processing time and ease of use in a single-step operation.

Circulating EVs in type 2 diabetes mellitus (T2DM)

Recent studies have provided novel mechanistic insights into circulating exosomes in T2DM.^{5,19,49} These studies also point to the need for purifying EVs with higher yield and without antibodies to elucidate their pathological effects. As a proof-of-concept for clinical testing, we isolate blood-borne EVs from healthy ($n = 5$) and T2DM ($n = 9$) subjects (Table S2[†]) using ExoDFF and UC. While EVs had similar size distribution regardless of the isolation methods according to nanoparticle tracking analysis (NTA) (Fig. S7[†]), EV counts were higher (per unit volume of whole blood) for T2DM patients as compared to healthy subjects with ExoDFF NV ($P < 0.05$) (Fig. 4A). ExoDFF MV, UC Exo and UC MV, although also showed higher EV counts for T2DM subjects, did not show any significant differences in EV count between both groups.

We next quantify the abundance of platelet-derived (CD41a+) and leukocyte-derived (CD45+) microvesicles in blood of healthy volunteers (non-fasted) for both ExoDFF MV and UC MV using flow cytometry. ExoDFF MV had significantly fewer platelet-derived microvesicles ($P < 0.05$) and more leukocyte-derived microvesicles ($P < 0.05$) than UC MV (Fig. S8A[†]). Lower leukocyte-derived microvesicles in UC MV samples could be attributed to multiple centrifugation steps (more EVs loss during manual handling) in contrast to the single-step ExoDFF operation. As UC MV samples had much higher and more heterogeneous platelet-derived microvesicles than ExoDFF MV, we performed additional experiments and found that the

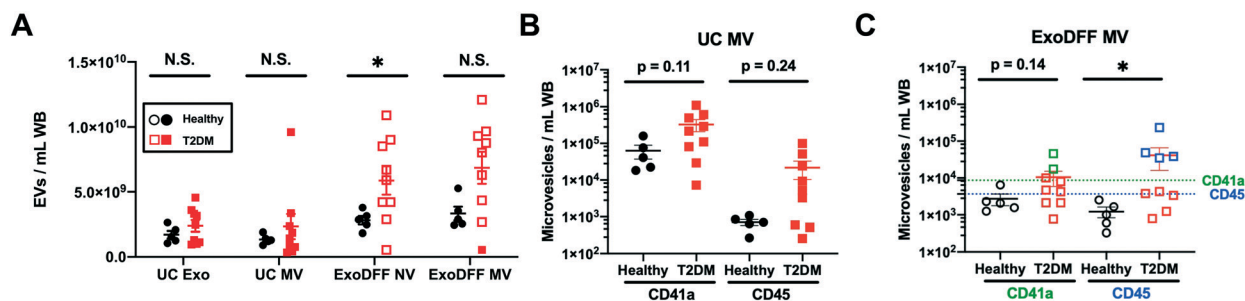


Fig. 4 Circulating EVs in T2DM. (A) Comparison of EV concentration (per mL of whole blood (WB)) isolated using ExoDFF and UC in healthy ($n = 5$) and T2DM subjects ($n = 9$). Quantification of platelet-derived (CD41a+) and leukocyte-derived (CD45+) microvesicles from healthy ($n = 5$) and T2DM ($n = 9$) subjects in (B) UC MV and (C) ExoDFF MV. For ExoDFF MV plot, dashed lines represent mean values for healthy subjects plus three standard deviations (CD41a green, CD45 blue). T2DM data points highlighted in green (two) and in blue (four) present abnormally high levels of platelet-derived and leukocyte-derived microvesicles, respectively. Data are presented using mean \pm s.e.m. * $p < 0.05$ and ** $p < 0.01$.

number of intact platelets (~ 2 to $3 \mu\text{m}$ in size) decreased significantly (by $\sim 84\%$) in platelet-rich plasma (PRP) after high speed centrifugation ($\sim 20\,000 \times g$, 45 min) in UC, while the pre-processed sample and ExoDFF (O3 and O4) platelet concentrations remained similar (Fig. S8B[†]). This indicates that there was minimal shear-induced platelet lysis using ExoDFF. Consequently, platelet-derived microvesicles ($< 1 \mu\text{m}$) count also varied greatly after UC in contrast to ExoDFF which showed negligible changes (Fig. S8C[†]). Taken together, these results indicate that ExoDFF is a more consistent method for immunophenotyping of microvesicles due to its gentle sorting of blood components (\sim maximum of $2000 \times g$ for ExoDFF vs. $\sim 20\,000 \times g$ for UC MV). The single-step operation helps to reduce losses of microvesicles derived from other cell types.

To test its clinical utility, we evaluated platelet-derived and leukocyte-derived microvesicles in healthy ($n = 5$) and T2DM ($n = 9$) subjects. For UC MV, we observed an increase in platelet-derived and leukocyte-derived microvesicles in T2DM subjects as compared to healthy subjects (Fig. 4B). Similarly, T2DM subjects also had higher platelet-derived and leukocyte-derived microvesicles ($P < 0.05$) for ExoDFF MV (Fig. 4C). We then defined healthy threshold (mean + 3S.D., 99.9% CI) values for microvesicles counts based on average and standard deviation of healthy subjects for ExoDFF MV. These results are graphically represented as green and blue dashed lines for CD41a and CD45, respectively. Based on these cut-offs, we identified two T2DM subjects (green squares) with abnormally high ($>$ ten-fold) levels of platelet-derived microvesicles, and four T2DM subjects (blue squares) with abnormally high ($>$ fifty-fold) levels of leukocyte-derived microvesicles, possibly indicating severe immune dysfunction. These subjects were collectively grouped as the “high risk” T2DM group to study EV-induced vascular inflammation.

Functional effects of healthy and diabetic EVs on vascular inflammation

To determine if EVs have any pathological effects on recipient cells, healthy and T2DM EVs (from UC Exo) were first labelled with PKH67 dye and incubated with human

umbilical vein endothelial cells (HUVEC) at different concentrations and for different durations (6 h and 24 h) to optimize treatment conditions (Fig. S9[†]). Based on flow cytometry and fluorescence imaging, the uptake of EVs by HUVEC was $\sim 95\%$ after 24 h when treated with $\sim 2.5 \times 10^9$ EVs per mL, regardless of their origin (from healthy or T2DM subjects) and was used as the treatment condition for *in vitro* vascular assays (Fig. 5A).

We next studied the functional effects of EVs extracted from healthy ($n = 5$), T2DM ($n = 3$), and “high risk” T2DM (T2DM high) ($n = 6$, determined based on results shown in Fig. 4C) using ExoDFF (ExoDFF NV and ExoDFF MV) and UC (UC Exo and UC MV) on HUVEC. Following incubation for 24 h, HUVEC were trypsinized and examined for ICAM-1 expression (inflammatory adhesion marker) using flow cytometry (Fig. 5B). “High risk” T2DM EVs induced a significant increase in ICAM-1 expression on HUVEC as compared to “non high-risk” T2DM ($P < 0.05$) and healthy ($P < 0.01$) EVs, regardless of the EV isolation method. There were negligible differences in endothelial ICAM-1 expression between healthy EV and T2DM EV treatment. Interestingly, there was also a significant increase in established cardiovascular risk factors including carotid intima-media thickness (CIMT) ($P < 0.01$), white blood cells (WBC) count ($P < 0.05$), and triglyceride level ($P < 0.05$) for “high risk” T2DM subjects as compared to healthy individuals (Fig. S10[†]). Hence, these results not only imply that ExoDFF-isolated EVs were functionally comparable to those from UC in mediating vascular inflammation, but also that immunophenotyping of ExoDFF MV could be a viable method and provide potential novel biomarkers for rapid vascular health risk stratification of T2DM patients. Secondly, it was also observed that HUVEC had higher ICAM-1 expression when treated with EVs from UC as compared to ExoDFF. A possible explanation could be attributed to the increase of platelet-derived microvesicles in UC Exo/MV. This observation is in agreement with prior work⁵⁰ documenting that platelet-derived EVs facilitate inflammation by adhering efficiently to EC to upregulate inflammatory markers.

To further validate this hypothesis, we isolated EVs using UC, ExoDFF and commercial size exclusion chromatography

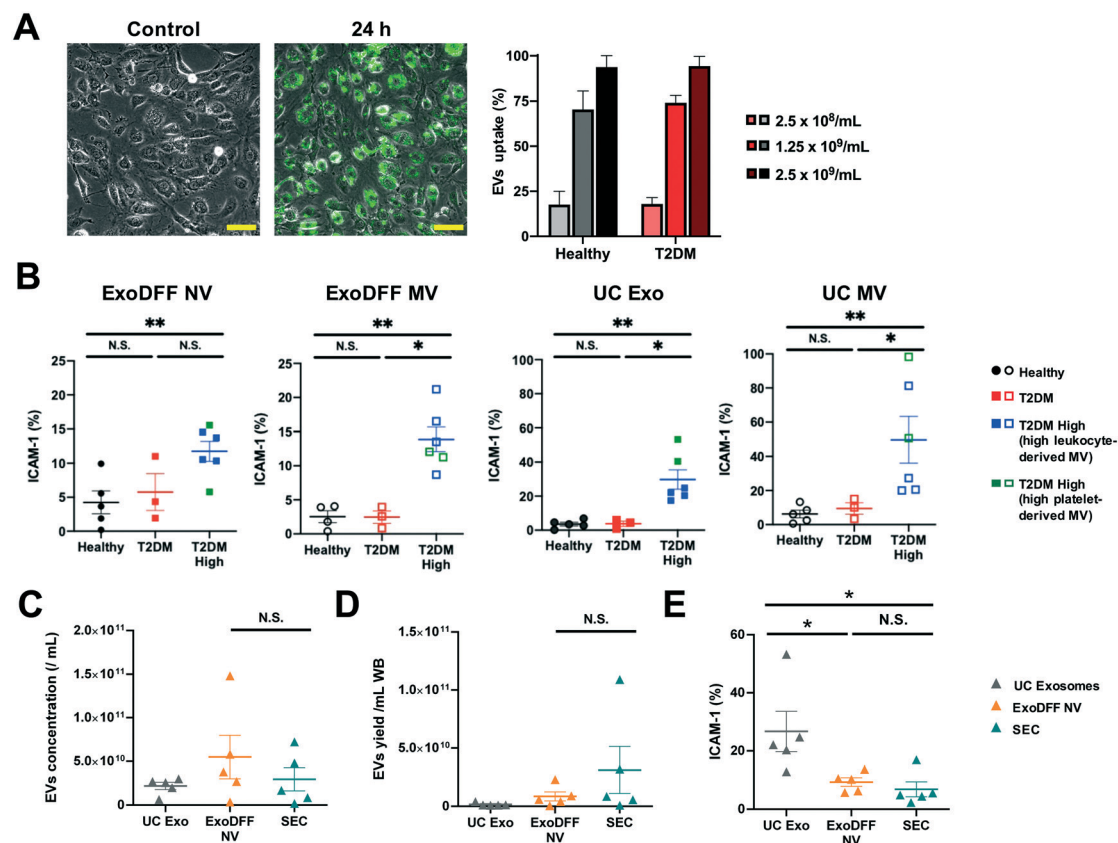


Fig. 5 Functional characterization of healthy and diabetic EVs on vascular inflammation. (A) Representative bright-field and fluorescence overlaid images of HUVEC monolayer incubated without (control) and with fluorescence-labelled EVs (PKH67) after 24 h. Scale bar: 50 μm . Plot illustrating the uptake of PKH67-stained EVs by HUVEC at varying concentrations after 24 h ($n = 3$). (B) Flow cytometry analysis of HUVEC ICAM-1 expressions after 24 h incubation with EVs isolated from healthy ($n = 5$), T2DM ($n = 3$) and “high risk” T2DM subjects ($n = 6$, T2DM high) using ExoDFF and UC. “High risk” T2DM data points highlighted in green and blue (determined from Fig. 4C) induced a significant increase in HUVEC ICAM-1 expression. Comparison of (C) EV concentration, (D) EV yield and (E) EV-induced HUVEC ICAM-1 expressions among three different isolation methods (UC, ExoDFF and SEC, $n = 5$). Data are presented as mean \pm s.e.m. * $p < 0.05$ and ** $p < 0.01$.

(SEC) in a subset of T2DM subjects ($n = 5$) to test for EVs-induced vascular inflammation. SEC is a chromatography-based method which isolates EVs based on size with efficient plasma protein depletion,⁵¹ and we have included this technique for comparison with ExoDFF and UC. While ExoDFF NV provided the highest concentration (Fig. 5C) of EVs, both ExoDFF and SEC were more efficient than UC in terms of EV yield (Fig. 5D), and EV sizes (Fig. S11[†]) between ExoDFF and SEC were also more similar. It should also be noted that SEC had higher EV yield than ExoDFF (although not statistically significant). Consistent with our earlier results, EV-induced ICAM-1 expression on HUVEC remained the highest using UC, which was significantly higher than ExoDFF ($P < 0.05$) and SEC ($P < 0.05$) (Fig. 5E). Taken together, these results indicate that both ExoDFF and SEC techniques are gentler than UC on EVs, which would be important to assess the functionality of EVs in their native state.

Multiplexed high throughput ExoDFF

Most microfluidic isolation technologies for micro- and nano-vesicles have limited scalability due to intricate

components that comprise integrated membranes and electrodes or complex instrumentation.^{27–29} To demonstrate increased processing throughput, we directly connected four ExoDFF subunits in parallel into a high throughput ExoDFF (ExoDFF^{HT}) multiplexed device (Fig. 6A). The positions of subunit spiral inlets and outlets were interchanged, and fluidic inlets from individual subunits were linked to two master inlets for sample and sheath fluid loading. Similar separation performance for polystyrene beads was observed in ExoDFF^{HT} with consistent separation of 50 nm beads into O1 (ExoDFF^{HT} NV) and 1 μm beads into O2 (waste outlet) in each spiral subunit (Fig. 6B). As expected, blood cells flow near the outer wall in each spiral subunit and they were efficiently sorted into the waste outlet at sample-to-sheath flow rate of 20:400 $\mu\text{L min}^{-1}$ per spiral device.

We next quantified the separation efficiency of 200 nm beads in ExoDFF and ExoDFF^{HT} devices using nanoparticle tracking analysis (NTA). There were negligible differences in the separation efficiencies for ExoDFF NV and ExoDFF^{HT} NV for sample-to-sheath flow rate of 20:400 (29% and 27.8%, respectively) as well as 40:400 (18% and 14.8%, respectively) (Fig. 6C). For whole blood characterization, the size

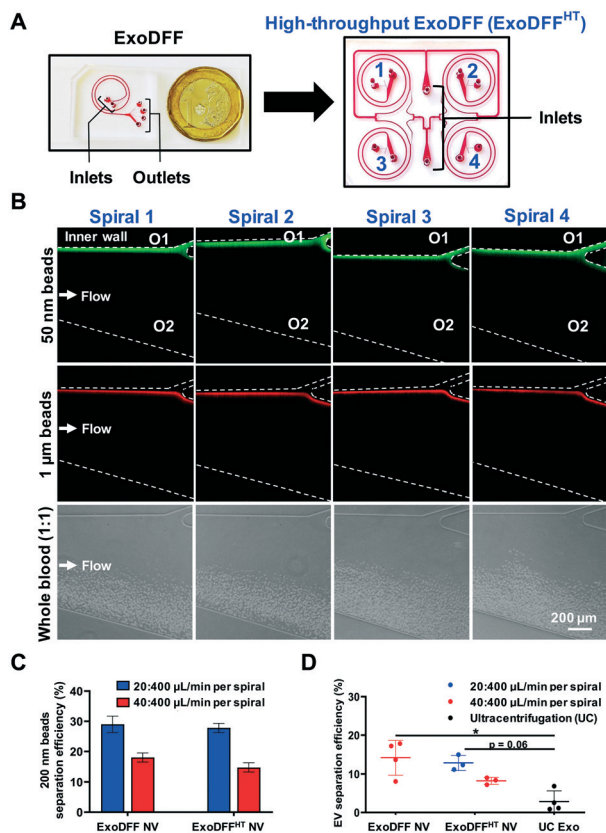


Fig. 6 Characterization of high throughput ExoDFF (ExoDFF^{HT}). (A) Multiplexing four ExoDFF devices into a single 2-inlet-8-outlet ExoDFF^{HT} device. (B) Fluorescent images indicating flow position and separation of 50 nm beads into O1 (ExoDFF^{HT} NV) and 1 μm beads into outlet 2 (waste outlet) at each spiral channel ($Re = 42$ at each spiral). High speed stacked images showing blood cells separation into O2 (waste outlet) at each spiral channel ($Re = 42$ at each spiral). (C) Quantification of 200 nm beads separation efficiency using ExoDFF and ExoDFF^{HT} at different sample to sheath flow rate ratio ($n = 3$). (D) Comparison of EV separation efficiencies from diluted whole blood (1:1) among ExoDFF, ExoDFF^{HT} and ultracentrifugation (UC) ($n = 3$). Data are presented as mean \pm s.d. * $p < 0.05$.

distribution profiles of EVs in the outlet (ExoDFF^{HT} NV) of each spiral subunit were similar (Fig. S12[†]), and the overall separation was $\sim 14\%$ for ExoDFF ($40:400 \mu\text{L min}^{-1}$) and ExoDFF^{HT} ($20:400 \mu\text{L min}^{-1}$) while efficiency decreased to 8.2% in ExoDFF^{HT} at $40:400 \mu\text{L min}^{-1}$ (Fig. 6D). A possible explanation is the stronger streamline dispersion into waste outlet in ExoDFF^{HT} due to the large channel resistance differences between EVs and waste outlets. Nevertheless, EV separation efficiency of ExoDFF^{HT} NV was three-fold higher than that of UC ($\sim 4\%$). Taken together, these results demonstrate the ability of our method to process up to $80 \mu\text{L}$ of whole blood per minute with ExoDFF^{HT}, which translates to processing $\sim 5 \text{ mL}$ of whole blood in an hour.

Discussion

In this work, we have developed a continuous-flow and scalable microfluidic technology (ExoDFF) for direct isolation

of circulating EVs from whole blood (1:1 dilution) based on the principles of Dean flow fractionation (DFF).³⁴ The spiral biochip offers unbiased (label-free) isolation of nanovesicles and microvesicles with its size-based and gentle function, which imposes an order of magnitude lower centrifugal force or g -force on the bioparticle than conventional ultracentrifugation. This method can also potentially minimize shear-induced damage or aggregation^{52,53} of EVs with short channel residence time ($\sim 0.12 \text{ s}$ vs. $\sim 10\text{--}15 \text{ min}$ EVs sedimentation time for UC).⁵⁴ By exploiting the subtle differences in transient Dean migration effects of the particles, we demonstrated separation of small micro- and nanoparticles ($a_p/D_h \sim 0.002$ to 0.02) which cannot be achieved otherwise in conventional inertial microfluidics devices.³⁵ With large channel dimensions ($D_h \sim 86 \mu\text{m}$) and lower operating flow rates ($Re \sim 40$), the present method significantly minimizes clogging issues and pressure-induced channel deformation.⁵⁵ Since it is a passive (hydrodynamic) sorting technique without the need for external force fields or functionalization with antibodies, the device cost and system setup (2 syringe pumps) effort are relatively lower. These advantages, together with the capability of direct blood-based EV isolation, are likely to render the device attractive for potential large-scale clinical studies with portability, automation, reproducibility and faster assay results.

While ExoDFF has a three-fold higher EV separation efficiency than UC, it is low compared to other microfluidic approaches.^{28,30} Two possible reasons are: the lack of standardized methods for quantification, and the high hematocrit in $2\times$ diluted whole blood sample ($20\text{--}25\%$). The latter may affect the Dean migration of small EVs towards the channel inner wall. Increasing sample blood dilution (reduced hematocrit) can potentially minimize crowding of RBCs to improve EV separation efficiency, but the trade-off would be reduced sample throughput. The current sample throughput for ExoDFF and ExoDFF^{HT} devices is $20 \mu\text{L min}^{-1}$ and $80 \mu\text{L min}^{-1}$ of whole blood, respectively, which translates to $\sim 1 \text{ h}$ processing time for 5 mL of blood. By simultaneously eluting small and medium-sized EVs into different outlets, this single-step operation can be automated to minimize human errors, and facilitate downstream assays (flow cytometry, nanoparticle tracking analysis (NTA) *etc.*), providing results within a few hours. Both ExoDFF and SEC give similar EV isolation performance, but it should be noted that plasma proteins or lipoproteins are co-eluted in ExoDFF NV/MV while SEC can remove proteins efficiently.⁵¹ Nevertheless, due to on-chip $10\times$ dilution by sheath buffer, protein background level in ExoDFF-isolated EVs is comparable to those of UC. As SEC cannot efficiently remove lipoproteins including LDL ($25\text{--}32 \text{ nm}$) and VLDL ($20\text{--}60 \text{ nm}$),^{56–58} density gradient UC will be necessary⁵⁹ although it is prone to significant losses of EVs. Asymmetrical flow field fractionation (AF4), a membrane-based crossflow filtration method, is currently the most sensitive EV sorting method with superior size resolution.⁵ However, its sample

throughput is low, and it is non-trivial to adopt it for large-scale clinical use. Hence, we envision ExoDFF to provide a unique first stage EV separation platform (potentially replacing UC). The present approach can be readily coupled with other EVs purification methods (Fig. S13†) for 2nd stage separation or specific EVs assays.

In T2DM, nearly all cell types related to vasculopathy including endothelial cells, leukocytes and platelets secrete EVs into the bloodstream to influence T2DM pathophysiology. Circulating endothelial^{16,60} and immune^{15,17} microvesicles in blood are increased in T2DM individuals, and are associated with cardiovascular risks.^{61,62} These studies mostly use high speed centrifugation to isolate microvesicles whereby the yield and quality are highly dependent on user operation. A major advantage of the present method is the direct isolation of circulating microvesicles from device outlet 2 (ExoDFF MV) without any centrifugation steps for rapid immunophenotyping by flow cytometry. This facilitates more accurate analysis of native microvesicle composition, which led to the identification of T2DM subjects with abnormal levels of platelet- and leukocytes-derived microvesicles (Fig. 4C).

In vitro and animal studies have reported that exosomes from diabetic subjects can modulate immune responses,⁶³ pancreatic B-cells⁶⁴ and vascular smooth muscle cells (VSMC).⁶⁵ Recent clinical efforts have also provided mechanistic insights into human diabetic exosomes including modulation of insulin resistance by microRNA transfer,^{49,66} upregulation of Exo-arginase I to reduce endothelial NO production,¹⁸ and increased leukocyte inflammation.¹⁹ In our study, we observed that ExoDFF-isolated EVs were functionally active, and diabetic EVs induced more vascular inflammation as compared to healthy EVs. Interestingly, the “high risk” T2DM individuals with abnormally high CD41a+ or CD45+ microvesicles (identified using ExoDFF MV) also had the most significant EVs-induced upregulation of endothelial ICAM-1 expressions, possibly indicating severe immune and vascular dysfunction (Fig. 5B). Due to the relatively small sample size in our pilot study, larger cohort studies are warranted for in-depth analysis of diabetic EVs and their associations with endothelial functions and different clinical presentations of diabetes. Nevertheless, these results provide evidence of EV-induced vascular inflammation in T2DM and point to the importance of EVs in diabetes-related vasculopathies, and their potential as non-traditional CVD biomarkers.

In summary, ExoDFF not only improves EV yield, but also reduces cost and processing time through automation and better accuracy. As endothelial dysfunction may precede the diagnosis of diabetes,⁶⁷ there is an unmet need to quantify vascular profile in healthy and T2DM individuals at early disease onset. We envision that the platform presented here will have numerous applications as a versatile research and clinical tool for EVs, and for combined immunological and functional phenotyping to formulate a novel blood-based testing strategy for vascular risk stratification in T2DM.

Author contributions

Hui Min Tay: conceptualization, data curation, formal analysis, investigation, methodology, validation, writing – original draft, writing – review & editing. Sheng Yuan Leong: conceptualization, methodology, software, validation, formal analysis, investigation, data curation, writing – original draft. Xiaohan Xu: formal analysis, investigation. Fang Kong: investigation, writing – original draft. Megha Upadya: investigation, writing – original draft. Rinkoo Dalan: conceptualization, methodology, resources. Chor Yong Tay: conceptualization. Ming Dao: conceptualization. Subra Suresh: conceptualization, methodology, supervision, writing – review & editing. Han Wei Hou: conceptualization, funding acquisition, methodology, project administration, supervision, resources, validation, writing – review & editing.

Conflicts of interest

There are no conflicts to declare.

Acknowledgements

H. W. H. would like to acknowledge the kind financial support from SMART Innovation Centre (ING-000539 BIO IGN and ING-001058 BIO IGN), Singapore Ministry of Education (MOE) Academic Research Fund Tier 1 (RG53/18), as well as A. Menarini Biomarkers Singapore Pte Ltd. S. Y. L would like to acknowledge support from the NTU Research Scholarship. We extend our thanks to Miss Siti Zaidah Binte Abu Bakar, Miss Yang Lulu and Miss Serene Chua Shu Xian from Tan Tock Seng Hospital, Singapore, for their assistance in patient recruitment and blood withdrawal. We also appreciate the guidance from Dr. Yumi Kawamura on exosomes isolation and analysis. S. S. is grateful to Nanyang Technological University for support through a Distinguished University Professorship.

References

- 1 M. Yáñez-Mó, P. R. Siljander, Z. Andreu, A. B. Zavec, F. E. Borràs, E. I. Buzas, K. Buzas, E. Casal, F. Cappello, J. Carvalho, E. Colás, A. Cordeiro-da Silva, S. Fais, J. M. Falcon-Perez, I. M. Ghobrial, B. Giebel, M. Gimona, M. Graner, I. Gursel, M. Gursel, N. H. Heegaard, A. Hendrix, P. Kierulf, K. Kokubun, M. Kosanovic, V. Kralj-Iglic, E. M. Krämer-Albers, S. Laitinen, C. Lässer, T. Lener, E. Ligeti, A. Linē, G. Lipps, A. Llorente, J. Lötvall, M. Manček-Keber, A. Marcilla, M. Mittelbrunn, I. Nazarenko, E. N. Nolte-t Hoen, T. A. Nyman, L. O'Driscoll, M. Olivan, C. Oliveira, É. Pállinger, H. A. Del Portillo, J. Reventós, M. Rigau, E. Rohde, M. Sammar, F. Sánchez-Madrid, N. Santarém, K. Schallmoser, M. S. Ostefeld, W. Stoorvogel, R. Stukelj, S. G. Van der Grein, M. H. Vasconcelos, M. H. Wauben and O. De Wever, *J. Extracell. Vesicles*, 2015, **4**, 27066.
- 2 G. Rabinowits, C. Gerçel-Taylor, J. M. Day, D. D. Taylor and G. H. Kloecker, *Clin. Lung Cancer*, 2009, **10**, 42–46.
- 3 G. Müller, *Diabetes, Metab. Syndr. Obes.: Targets Ther.*, 2012, **5**, 247–282.

- 4 S. J. Gould and G. Raposo, *J. Extracell. Vesicles*, 2013, **2**, 20389.
- 5 H. Zhang, D. Freitas, H. S. Kim, K. Fabijanic, Z. Li, H. Chen, M. T. Mark, H. Molina, A. B. Martin, L. Bojmar, J. Fang, S. Rampersaud, A. Hoshino, I. Matei, C. M. Kenific, M. Nakajima, A. P. Mutvei, P. Sansone, W. Buehring, H. Wang, J. P. Jimenez, L. Cohen-Gould, N. Paknejad, M. Brendel, K. Manova-Todorova, A. Magalhães, J. A. Ferreira, H. Osório, A. M. Silva, A. Massey, J. R. Cubillos-Ruiz, G. Galletti, P. Giannakakou, A. M. Cuervo, J. Blenis, R. Schwartz, M. S. Brady, H. Peinado, J. Bromberg, H. Matsui, C. A. Reis and D. Lyden, *Nat. Cell Biol.*, 2018, **20**, 332–343.
- 6 T. Baranyai, K. Herczeg, Z. Onodi, I. Voszka, K. Modos, N. Marton, G. Nagy, I. Mager, M. J. Wood, S. El Andaloussi, Z. Palinkas, V. Kumar, P. Nagy, A. Kittel, E. I. Buzas, P. Ferdinandy and Z. Giricz, *PLoS One*, 2015, **10**, e0145686.
- 7 W. Wang, J. Luo and S. Wang, *Adv. Healthcare Mater.*, 2018, **7**, e1800484.
- 8 G. K. Patel, M. A. Khan, H. Zubair, S. K. Srivastava, M. D. Khushman, S. Singh and A. P. Singh, *Sci. Rep.*, 2019, **9**, 5335.
- 9 V. Sunkara, C.-J. Kim, J. Park, H.-K. Woo, D. Kim, H. K. Ha, M.-H. Kim, Y. Son, J.-R. Kim and Y.-K. Cho, *Theranostics*, 2019, **9**, 1851–1863.
- 10 S. Boukouris and S. Mathivanan, *Proteomics: Clin. Appl.*, 2015, **9**, 358–367.
- 11 M. Li, E. Zeringer, T. Barta, J. Schageman, A. Cheng and A. V. Vlassov, *Philos. Trans. R. Soc., B*, 2014, **369**, 20130502.
- 12 V. L. Roger, A. S. Go, D. M. Lloyd-Jones, E. J. Benjamin, J. D. Berry, W. B. Borden, D. M. Bravata, S. Dai, E. S. Ford, C. S. Fox, H. J. Fullerton, C. Gillespie, S. M. Hailpern, J. A. Heit, V. J. Howard, B. M. Kissela, S. J. Kittner, D. T. Lackland, J. H. Lichtman, L. D. Lisabeth, D. M. Makuc, G. M. Marcus, A. Marelli, D. B. Matchar, C. S. Moy, D. Mozaffarian, M. E. Mussolino, G. Nichol, N. P. Paynter, E. Z. Soliman, P. D. Sorlie, N. Sotoodehnia, T. N. Turan, S. S. Virani, N. D. Wong, D. Woo and M. B. Turner, *Circulation*, 2012, **125**, 188–197.
- 13 N. Sarwar, P. Gao, S. R. Seshasai, R. Gobin, S. Kaptoge, E. Di Angelantonio, E. Ingelsson, D. A. Lawlor, E. Selvin, M. Stampfer, C. D. Stehouwer, S. Lewington, L. Pennells, A. Thompson, N. Sattar, I. R. White, K. K. Ray and J. Danesh, *Lancet*, 2010, **375**, 2215–2222.
- 14 C. M. Boulanger, A. Scoazec, T. Ebrahimian, P. Henry, E. Mathieu, A. Tedgui and Z. Mallat, *Circulation*, 2001, **104**, 2649–2652.
- 15 F. Sabatier, P. Darmon, B. Hugel, V. Combes, M. Sanmarco, J.-G. Velut, D. Arnoux, P. Charpiot, J.-M. Freyssinet, C. Oliver, J. Sampol and F. Dignat-George, *Diabetes*, 2002, **51**, 2840–2845.
- 16 H. Koga, S. Sugiyama, K. Kugiyama, K. Watanabe, H. Fukushima, T. Tanaka, T. Sakamoto, M. Yoshimura, H. Jinnouchi and H. Ogawa, *J. Am. Coll. Cardiol.*, 2005, **45**, 1622–1630.
- 17 B. Feng, Y. Chen, Y. Luo, M. Chen, X. Li and Y. Ni, *Atherosclerosis*, 2010, **208**, 264–269.
- 18 H. Zhang, J. Liu, D. Qu, L. Wang, C. M. Wong, C.-W. Lau, Y. Huang, Y. F. Wang, H. Huang, Y. Xia, L. Xiang, Z. Cai, P. Liu, Y. Wei, X. Yao, R. C. W. Ma and Y. Huang, *Proc. Natl. Acad. Sci. U. S. A.*, 2018, **115**, E6927–E6936.
- 19 D. W. Freeman, N. Noren Hooten, E. Eitan, J. Green, N. A. Mode, M. Bodogai, Y. Zhang, E. Lehrmann, A. B. Zonderman, A. Biragyn, J. Egan, K. G. Becker, M. P. Mattson, N. Ejiogu and M. K. Evans, *Diabetes*, 2018, **67**, 2377–2388.
- 20 S. Busatto, G. Vilanilam, T. Ticer, W. L. Lin, D. W. Dickson, S. Shapiro, P. Bergese and J. Wolfram, *Cell*, 2018, **7**, 273.
- 21 H. Zhang and D. Lyden, *Nat. Protoc.*, 2019, **14**, 1027–1053.
- 22 L. S. Gaspar, M. M. Santana, C. Henriques, M. M. Pinto, T. M. Ribeiro-Rodrigues, H. Girão, R. J. Nobre and L. Pereira de Almeida, *Mol. Ther.–Methods Clin. Dev.*, 2020, **18**, 723–737.
- 23 K. Sidhom, P. O. Obi and A. Saleem, *Int. J. Mol. Sci.*, 2020, **21**, 6466.
- 24 F. Liu, O. Vermesh, V. Mani, T. J. Ge, S. J. Madsen, A. Sabour, E. C. Hsu, G. Gowrishankar, M. Kanada, J. V. Jokerst, R. G. Sierra, E. Chang, K. Lau, K. Sridhar, A. Bermudez, S. J. Pitteri, T. Stoyanova, R. Sinclair, V. S. Nair, S. S. Gambhir and U. Demirci, *ACS Nano*, 2017, **11**, 10712–10723.
- 25 B. H. Wunsch, J. T. Smith, S. M. Gifford, C. Wang, M. Brink, R. L. Bruce, R. H. Austin, G. Stolovitzky and Y. Astier, *Nat. Nanotechnol.*, 2016, **11**, 936–940.
- 26 C. Liu, J. Guo, F. Tian, N. Yang, F. Yan, Y. Ding, J. Wei, G. Hu, G. Nie and J. Sun, *ACS Nano*, 2017, **11**, 6968–6976.
- 27 K. Lee, H. Shao, R. Weissleder and H. Lee, *ACS Nano*, 2015, **9**, 2321–2327.
- 28 M. Wu, Y. Ouyang, Z. Wang, R. Zhang, P. H. Huang, C. Chen, H. Li, P. Li, D. Quinn, M. Dao, S. Suresh, Y. Sadosky and T. J. Huang, *Proc. Natl. Acad. Sci. U. S. A.*, 2017, **114**, 10584–10589.
- 29 S. D. Ibsen, J. Wright, J. M. Lewis, S. Kim, S. Y. Ko, J. Ong, S. Manouchehri, A. Vyas, J. Akers, C. C. Chen, B. S. Carter, S. C. Esener and M. J. Heller, *ACS Nano*, 2017, **11**, 6641–6651.
- 30 P. Zhang, X. Zhou, M. He, Y. Shang, A. L. Tetlow, A. K. Godwin and Y. Zeng, *Nat. Biomed. Eng.*, 2019, **3**, 438–451.
- 31 E. Reátegui, K. E. van der Vos, C. P. Lai, M. Zeinali, N. A. Atai, B. Aldikacti, F. P. Floyd Jr., A. H. Khankhel, V. Thapar, F. H. Hochberg, L. V. Sequist, B. V. Nahed, B. S. Carter, M. Toner, L. Balaj, D. T. Ting, X. O. Breakefield and S. L. Stott, *Nat. Commun.*, 2018, **9**, 175.
- 32 H. W. Hou, M. E. Warkiani, B. L. Khoo, Z. R. Li, R. A. Soo, D. S.-W. Tan, W.-T. Lim, J. Han, A. A. S. Bhagat and C. T. Lim, *Sci. Rep.*, 2013, **3**, 1259.
- 33 H. W. Hou, C. Petchakup, H. M. Tay, Z. Y. Tam, R. Dalan, D. E. Chew, K. H. Li and B. O. Boehm, *Sci. Rep.*, 2016, **6**, 29410.
- 34 H. M. Tay, S. Kharel, R. Dalan, Z. J. Chen, K. K. Tan, B. O. Boehm, S. C. J. Loo and H. W. Hou, *NPG Asia Mater.*, 2017, **9**, e434.
- 35 D. Di Carlo, D. Irimia, R. G. Tompkins and M. Toner, *Proc. Natl. Acad. Sci. U. S. A.*, 2007, **104**, 18892–18897.
- 36 H. Amini, W. Lee and D. Di Carlo, *Lab Chip*, 2014, **14**, 2739–2761.
- 37 D. Di Carlo, *Lab Chip*, 2009, **9**, 3038–3046.
- 38 A. J. Chung, *BioChip J.*, 2019, **13**, 53–63.

- 39 M. Masaeli, E. Sollier, H. Amini, W. Mao, K. Camacho, N. Doshi, S. Mitragotri, A. Alexeev and D. Di Carlo, *Phys. Rev. X*, 2012, 2, 031017.
- 40 M. Li, H. E. Muñoz, K. Goda and D. Di Carlo, *Sci. Rep.*, 2017, 7, 10802.
- 41 S. C. Hur, N. K. Henderson-MacLennan, E. R. B. McCabe and D. Di Carlo, *Lab Chip*, 2011, 11, 912–920.
- 42 E. Guźniczak, O. Otto, G. Whyte, N. Willoughby, M. Jimenez and H. Bridle, *Lab Chip*, 2020, 20, 614–625.
- 43 J. M. Martel and M. Toner, *Sci. Rep.*, 2013, 3, 3340.
- 44 Y. Ying and Y. Lin, *Sci. Rep.*, 2019, 9, 16575.
- 45 A. A. S. Bhagat, S. S. Kuntaegowdanahalli and I. Papautsky, *Lab Chip*, 2008, 8, 1906–1914.
- 46 K. W. Witwer, E. I. Buzás, L. T. Bemis, A. Bora, C. Lässer, J. Lötvall, E. N. Nolte-t Hoen, M. G. Piper, S. Sivaraman, J. Skog, C. Théry, M. H. Wauben and F. Hochberg, *J. Extracell. Vesicles*, 2013, 2, 20360.
- 47 S. T.-Y. Chuo, J. C.-Y. Chien and C. P.-K. Lai, *J. Biomed. Sci.*, 2018, 25, 91.
- 48 Y. Kawamura, A. Sanchez Calle, Y. Yamamoto, T. A. Sato and T. Ochiya, *J. Extracell. Vesicles*, 2019, 8, 1643214.
- 49 W. Ying, M. Riopel, G. Bandyopadhyay, Y. Dong, A. Birmingham, J. B. Seo, J. M. Ofrecio, J. Wollam, A. Hernandez-Carretero, W. Fu, P. Li and J. M. Olefsky, *Cell*, 2017, 171, 372–384.e312.
- 50 S. J. Kuravi, P. Harrison, G. E. Rainger and G. B. Nash, *Inflammation*, 2019, 42, 290–305.
- 51 A. Gámez-Valero, M. Monguío-Tortajada, L. Carreras-Planella, M. L. Franquesa, K. Beyer and F. E. Borràs, *Sci. Rep.*, 2016, 6, 33641.
- 52 E. A. Mol, M.-J. Goumans, P. A. Doevendans, J. P. G. Sluiter and P. Vader, *Nanomedicine*, 2017, 13, 2061–2065.
- 53 G. Corso, I. Mäger, Y. Lee, A. Görgens, J. Bultema, B. Giebel, M. J. A. Wood, J. Z. Nordin and S. E. L. Andaloussi, *Sci. Rep.*, 2017, 7, 11561.
- 54 M. A. Livshits, E. Khomyakova, E. G. Evtushenko, V. N. Lazarev, N. A. Kulemin, S. E. Semina, E. V. Generozov and V. M. Govorun, *Sci. Rep.*, 2015, 5, 17319.
- 55 E. Sollier, C. Murray, P. Maoddi and D. Di Carlo, *Lab Chip*, 2011, 11, 3752–3765.
- 56 R. Stranska, L. Gysbrechts, J. Wouters, P. Vermeersch, K. Bloch, D. Dierickx, G. Andrei and R. Snoeck, *J. Transl. Med.*, 2018, 16, 1.
- 57 N. Karimi, A. Cvjetkovic, S. C. Jang, R. Crescitelli, M. A. Hosseinpour Feizi, R. Nieuwland, J. Lötvall and C. Lässer, *Cell. Mol. Life Sci.*, 2018, 75, 2873–2886.
- 58 M. Mørk, M. H. Nielsen, R. Bæk, M. M. Jørgensen, S. Pedersen and S. R. Kristensen, *TH Open*, 2018, 2, e147–e157.
- 59 C. Thery, K. W. Witwer, E. Aikawa, M. J. Alcaraz, J. D. Anderson, R. Andriantsitohaina, A. Antoniou, T. Arab, F. Archer, G. K. Atkin-Smith, D. C. Ayre, J. M. Bach, D. Bachurski, H. Baharvand, L. Balaj, S. Baldacchino, N. N. Bauer, A. A. Baxter, M. Bebawy, C. Beckham, A. B. Zavec, A. Benmoussa, A. C. Berardi, P. Bergese, E. Bielska, C. Blenkins, S. Bobis-Wozowicz, E. Boilard, W. Boireau, A. Bongiovanni, F. E. Borràs, S. Bosch, C. M. Boulanger, X. Breakefield, A. M. Breglio, M. A. Brennan, D. R. Brigstock, A. Brisson, M. L. Broekman, J. F. Bromberg, P. Bryl-Gorecka, S. Buch, A. H. Buck, D. Burger, S. Busatto, D. Buschmann, B. Bussolati, E. I. Buzas, J. B. Byrd, G. Camussi, D. R. Carter, S. Caruso, L. W. Chamley, Y. T. Chang, C. Chen, S. Chen, L. Cheng, A. R. Chin, A. Clayton, S. P. Clerici, A. Cocks, E. Cocucci, R. J. Coffey, A. Cordeiro-da-Silva, Y. Couch, F. A. Coumans, B. Coyle, R. Crescitelli, M. F. Criado, C. D'Souza-Schorey, S. Das, A. D. Chaudhuri, P. de Candia, E. F. De Santana, O. De Wever, H. A. Del Portillo, T. Demaret, S. Deville, A. Devitt, B. Dhondt, D. Di Vizio, L. C. Dieterich, V. Dolo, A. P. D. Rubio, M. Dominici, M. R. Dourado, T. A. Driedonks, F. V. Duarte, H. M. Duncan, R. M. Eichenberger, K. Ekstrom, S. El Andaloussi, C. Elie-Caille, U. Erdbrugger, J. M. Falcon-Perez, F. Fatima, J. E. Fish, M. Flores-Bellver, A. Forsonits, A. Frelet-Barrand, F. Fricke, G. Fuhrmann, S. Gabrielsson, A. Gamez-Valero, C. Gardiner, K. Gartner, R. Gaudin, Y. S. Gho, B. Giebel, C. Gilbert, M. Gimona, I. Giusti, D. C. Goberdhan, A. Gorgens, S. M. Gorski, D. W. Greening, J. C. Gross, A. Gualerzi, G. N. Gupta, D. Gustafson, A. Handberg, R. A. Haraszti, P. Harrison, H. Hegyesi, A. Hendrix, A. F. Hill, F. H. Hochberg, K. F. Hoffmann, B. Holder, H. Holthofer, B. Hosseinkhani, G. Hu, Y. Huang, V. Huber, S. Hunt, A. G. Ibrahim, T. Ikezu, J. M. Inal, M. Isin, A. Ivanova, H. K. Jackson, S. Jacobsen, S. M. Jay, M. Jayachandran, G. Jenster, L. Jiang, S. M. Johnson, J. C. Jones, A. Jong, T. Jovanovic-Taliman, S. Jung, R. Kalluri, S. I. Kano, S. Kaur, Y. Kawamura, E. T. Keller, D. Khamari, E. Khomyakova, A. Khvorova, P. Kierulf, K. P. Kim, T. Kislinger, M. Klingeborn, D. J. Klinke, M. Kornek, M. M. Kosanovic, A. F. Kovacs, E. M. Kramer-Albers, S. Krasemann, M. Krause, I. V. Kurochkin, G. D. Kusuma, S. Kuypers, S. Laitinen, S. M. Langevin, L. R. Languino, J. Lannigan, C. Lasser, L. C. Laurent, G. Lavieu, E. Lazaro-Ibanez, S. Le Lay, M. S. Lee, Y. X. F. Lee, D. S. Lemos, M. Lenassi, A. Leszczynska, I. T. Li, K. Liao, S. F. Libregts, E. Ligeti, R. Lim, S. K. Lim, A. Line, K. Linnemannstons, A. Llorente, C. A. Lombard, M. J. Lorenowicz, A. M. Lorincz, J. Lotvall, J. Lovett, M. C. Lowry, X. Loyer, Q. Lu, B. Lukomska, T. R. Lunavat, S. L. Maas, H. Malhi, A. Marcilla, J. Mariani, J. Mariscal, E. S. Martens-Uzunova, L. Martin-Jaular, M. C. Martinez, V. R. Martins, M. Mathieu, S. Mathivanan, M. Maugeri, L. K. McGinnis, M. J. McVey, D. G. Meckes Jr., K. L. Meehan, I. Mertens, V. R. Minciocchi, A. Moller, M. M. Jørgensen, A. Morales-Kastresana, J. Morhayim, F. Mullier, M. Muraca, L. Musante, V. Mussack, D. C. Muth, K. H. Myburgh, T. Najrana, M. Nawaz, I. Nazarenko, P. Nejsun, C. Neri, T. Neri, R. Nieuwland, L. Nimrichter, J. P. Nolan, E. N. Nolte-t Hoen, N. N. Hooten, L. O'Driscoll, T. O'Grady, A. O'Loughlen, T. Ochiya, M. Olivier, A. Ortiz, L. A. Ortiz, X. Osteikoetxea, O. Ostergaard, M. Ostrowski, J. Park, D. M. Pegtel, H. Peinado, F. Perut, M. W. Pfaffl, D. G. Phinney, B. C. Pieters, R. C. Pink, D. S. Pisetsky, E. P. von Strandmann, I. Polakovicova, I. K. Poon, B. H. Powell, I. Prada, L. Pulliam, P.

- Quesenberry A, Radeghieri, R. L. Raffai, S. Raimondo, J. Rak, M. I. Ramirez, G. Raposo, M. S. Rayyan, N. Regev-Rudzki, F. L. Ricklefs, P. D. Robbins, D. D. Roberts, S. C. Rodrigues, E. Rohde, S. Rome, K. M. Rouschop, A. Rughetti, A. E. Russell, P. Saa, S. Sahoo, E. Salas-Huenuleo, C. Sanchez, J. A. Saugstad, M. J. Saul, R. M. Schiffelers, R. Schneider, T. H. Schoyen, A. Scott, E. Shahaj, S. Sharma, O. Shatnyeva, F. Shekari, G. V. Shelke, A. K. Shetty, K. Shiba, P. R. Siljander, A. M. Silva, A. Skowronek, O. L. Snyder, R. P. Soares, B. W. Sodar, C. Soekmadji, J. Sotillo, P. D. Stahl, W. Stoorvogel, S. L. Stott, E. F. Strasser, S. Swift, H. Tahara, M. Tewari, K. Timms, S. Tiwari, R. Tixeira, M. Tkach, W. S. Toh, R. Tomasini, A. C. Torrecilhas, J. P. Tosar, V. Toxavidis, L. Urbanelli, P. Vader, B. W. van Balkom, S. G. van der Grein, J. Van Deun, M. J. van Herwijnen, K. Van Keuren-Jensen, G. van Niel, M. E. van Royen, A. J. van Wijnen, M. H. Vasconcelos, I. J. Vechetti Jr., T. D. Veit, L. J. Vella, E. Velot, F. J. Verweij, B. Vestad, J. L. Vinas, T. Visnovitz, K. V. Vukman, J. Wahlgren, D. C. Watson, M. H. Wauben, A. Weaver, J. P. Webber, V. Weber, A. M. Wehman, D. J. Weiss, J. A. Welsh, S. Wendt, A. M. Wheelock, Z. Wiener, L. Witte, J. Wolfram, A. Xagorari, P. Xander, J. Xu, X. Yan, M. Yanez-Mo, H. Yin, Y. Yuana, V. Zappulli, J. Zarubova, V. Zekas, J. Y. Zhang, Z. Zhao, L. Zheng, A. R. Zheutlin, A. M. Zickler, P. Zimmermann, A. M. Zivkovic, D. Zocco and E. K. Zuba-Surma, *J. Extracell. Vesicles*, 2018, **7**, 1535750.
- 60 A. F. Tramontano, R. Lyubarova, J. Tsiakos, T. Palaia, J. R. Deleon and L. Ragolia, *Mediators Inflammation*, 2010, **2010**, 250476.
- 61 A. M. Curtis, L. Zhang, E. Medenilla, M. Gui, P. F. Wilkinson, E. Hu, J. Giri, V. Doraiswamy, S. Gunda, M. E. Burgert, J. S. Moore, J. M. Edelberg and E. R. Mohler III, *Cytometry, Part B*, 2010, **78**, 329–337.
- 62 T. Nozaki, S. Sugiyama, H. Koga, K. Sugamura, K. Ohba, Y. Matsuzawa, H. Sumida, K. Matsui, H. Jinnouchi and H. Ogawa, *J. Am. Coll. Cardiol.*, 2009, **54**, 601–608.
- 63 Z. B. Deng, A. Poliakov, R. W. Hardy, R. Clements, C. Liu, Y. Liu, J. Wang, X. Xiang, S. Zhang, X. Zhuang, S. V. Shah, D. Sun, S. Michalek, W. E. Grizzle, T. Garvey, J. Mobley and H. G. Zhang, *Diabetes*, 2009, **58**, 2498–2505.
- 64 A. Jalabert, G. Vial, C. Guay, O. P. Wiklander, J. Z. Nordin, H. Aswad, A. Forterre, E. Meugnier, S. Pesenti, R. Regazzi, E. Danty-Berger, S. Ducreux, H. Vidal, S. El-Andaloussi, J. Rieusset and S. Rome, *Diabetologia*, 2016, **59**, 1049–1058.
- 65 S. Li, J.-K. Zhan, Y.-J. Wang, X. Lin, J.-Y. Zhong, Y. Wang, P. Tan, J.-Y. He, X.-J. Cui, Y.-Y. Chen, W. Huang and Y.-S. Liu, *Cell Biosci.*, 2019, **9**, 1.
- 66 M. Katayama, O. P. B. Wiklander, T. Fritz, K. Caidahl, S. El-Andaloussi, J. R. Zierath and A. Krook, *Diabetes*, 2019, **68**, 515–526.
- 67 B. M. Balletshofer, K. Rittig, M. D. Enderle, A. Volk, E. Maerker, S. Jacob, S. Matthaei, K. Rett and H. U. Häring, *Circulation*, 2000, **101**, 1780–1784.

Supporting Information

Direct Isolation of Circulating Extracellular Vesicles from Blood for Vascular Risk Profiling in Type 2 Diabetes Mellitus

Hui Min Tay, Sheng Yuan Leong, Xiaohan Xu, Fang Kong, Megha Upadya, Rinkoo Dalan, Chor Yong Tay, Ming Dao, Subra Suresh* and Han Wei Hou*

Materials and Methods

Microfluidic Device Fabrication

The 2-inlet, 4-outlet ExoDFF device, shown in Figure 1, was fabricated with poly-dimethylsiloxane (PDMS; Dow Corning, Midland, MI, USA) using standard soft lithography methods. PDMS prepolymer was mixed well with the curing agent in a ratio of 10:1 (w/w) and poured over a silicon wafer patterned with ExoDFF design. The mixture was de-gassed before curing in an oven at 80 °C for 2 h. The cured PDMS slab was carefully peeled from the wafer, and inlets and outlet holes were punched out with a 1.5 mm biopsy puncher. The PDMS slab was cleaned thoroughly with isopropanol and bonded to a 1 mm thick glass slide (70 mm × 50 mm) using an air plasma machine (PDC-002, Harrick Plasma Inc, Ithaca, NY, USA).

Computational Fluid Dynamics (CFD) Simulation

Computation fluid dynamics simulation was conducted using ANSYS FLUENT (Canonsburg, PA, USA). Steady state pressure-based laminar flow was analyzed using SIMPLE scheme. Fluid is modelled as water to mimic PBS. A complete hexahedral discretization mesh was built using ANSYS ICEM CFD (Canonsburg, PA, USA) with maximum element dimension of 2 µm along height and width directions, 25 µm along length direction. Determinant, maximum orthogonality and maximum warpage of element was set to minimum value of 0.3. Only upper half of the channel was modelled due to symmetry in height direction. Boundary conditions were set to velocity inlet, zero gauge pressure outlet, and no slip at channel walls. 1000 fluid streamlines were initiated from sample inlet using discrete phase model (DPM) without interaction with the continuous phase. Coordinates of streamlines were then exported and processed with MATLAB (MathWorks, Natick, MA, USA). Total flow rate was set to 480 µL/min with different sample to sheath flow rate ratio ranging from 1:3 to 1:40.

Western Blot

Equal volume (15 µL) of ExoDFF outlets, UC microvesicles (UC MV) and UC exosomes (UC Exo) and a reduced volume (0.5 µL) of plasma were lysed in Radioimmunoprecipitation assay (RIPA) buffer (Pierce, Thermo Scientific) containing protease inhibitor cocktail (Thermo Scientific) with the samples chilled on ice. The samples were mixed with loading buffer containing β-mercaptoethanol (Merck, Darmstadt, Germany), heated to 70 °C for 10 min, loaded on 15% SDS-PAGE gels and electrophoresed to detect exosome markers CD9, Flotillin-1 and TSG101. Proteins were transferred to 0.45 µm nitrocellulose membranes (Bio-rad, Feldkirchen, Germany) and stained with REVERT total protein stain (Li-COR Biosciences, Lincoln, NE, USA) for normalisation. Membranes were blocked for 1 h with Odyssey blocking buffer TBS (Li-COR Biosciences, Lincoln, NE, USA) at room temperature, and incubated with 1:1000 of the following antibodies - Rabbit monoclonal [EPR2949] anti-CD9 (Abcam ab92726); mouse monoclonal anti-Flotillin-1 (C2) (Santa Cruz Biotechnology, sc-74566, Dallas, TX, USA) and mouse monoclonal [4A10] anti-TSG101 (Abcam, ab83, Cambridge, MA, USA) overnight at 4 °C. The membranes were next washed using 1X Tris Buffered Saline (TBS) 0.1% Tween 20 (TBS-T), and incubated with 1:15,000 each of IRDye 800CW anti-mouse IgG secondary antibody (Li-COR Biosciences, Lincoln, NE, USA) and IRDye 680LT anti-rabbit IgG secondary antibody (Li-COR Biosciences, Lincoln, NE, USA) for 1 h at room temperature. Membranes were washed again with 1X TBS-T and

scanned with an Odyssey CLx imaging system (Li-COR Biosciences) using 700- and 800-nm channels and visualized using ImageStudio software version 5.2 (LI-COR Biosciences).

RNA Isolation and Measurement

Total RNA was extracted from extracellular vesicles using miRNeasy Mini Kit (Qiagen, Venlo, Netherlands) according to the manufacturer's protocol. The purity and concentration of the isolated RNA were measured using NanoDrop One Microvolume UV-Vis Spectrophotometer (ND-ONE-W, Thermo Scientific) and RNA size distribution was analysed using 2100 Bioanalyzer System (Agilent, Santa Clara, CA, USA) with the RNA 6000 Pico Kit according to the manufacturer's protocol.

Cell Culture

Human umbilical vein endothelial cells (HUVEC; Lonza) were cultured in endothelial cell growth medium (EGM-2; Lonza) supplemented with 1% penicillin-streptomycin (P/S; Gibco, Grand Island, NY, USA) in a T75 flask. The cells were maintained at 37 °C in a humidified 5% CO₂ incubator and medium was changed thrice weekly. For EVs uptake assay, confluent HUVEC was dissociated using 0.25% trypsin with 1 mM EDTA (Gibco) and seeded in a 24-well plate at 8×10^4 cells per well with 400 μ L EGM-2 and grown to confluency prior use.

Platelet Count and Platelet-derived Microvesicles

To examine the platelet shearing effects of centrifugation, whole blood was first centrifuged at 1,000 g for 5 min to obtain platelet rich plasma (PRP). The PRP was then either subjected to high speed centrifugation at 20,000 x g for 45 min or perfused into ExoDFF device for sorting. Pre-processed PRP sample, pellet from high speed centrifugation and ExoDFF fractions (O2 for platelet-derived microvesicles, O3 – O4 for platelets) were then stained with FITC-conjugated anti-human CD41a antibody to detect and compare intact residual platelets and CD41a+ microvesicles using flow cytometry.

Transmission Electron Microscopy (TEM)

EVs isolated from ExoDFF were subjected to SEC to remove plasma proteins before TEM analysis. For TEM analysis, a carbon-coated grid (CF300-CU, Electron Microscopy Sciences, Hatfield, PA, USA) was glow-discharged for 1 min. A 4 μ L of sample solution was then placed on the grid to adsorb for 1 min. After blotting, 4 μ L of 2% uranyl acetate was added to the grid to negatively stain the sample for 1 min. The grid was then blotted and air-dried. Grids were imaged using a T12 Icorr transmission electron microscope operating at 120 kV. Images were captured by an Eagle 4k HS camera.

EV Uptake Assay

To optimize EV concentration for cell uptake assay, UC isolated exosomes (UC Exo) and microvesicles (UC MV) were first stained with 2 μ M PKH67 dye in Diluent C (Sigma Aldrich, St. Louis, MO, USA), washed, and incubated separately with HUVEC at varying concentration and duration. The stained EV uptake was examined using fluorescent microscopy and flow cytometry, and optimal uptake condition is determined to be 2.5×10^9 EVs per mL for 24 h. EVs isolated from clinical samples with UC and ExoDFF were then directly incubated with HUVEC as previously described, and the treated HUVEC were trypsinized and examined for inflammatory marker ICAM-1 expression using flow cytometry analysis.

Size Exclusion Chromatography (SEC)

To isolate EVs from plasma by SEC, PURE-EVs columns (HBM-PEV, HansaBioMed Life Sciences, Tallinn, Estonia) were used according to the manufacturer's instructions. The column was first washed three times with 10 mL PBS to eliminate preservative buffer residues and then 500 μ L of platelet poor plasma (PPP) was applied onto the column. During the elution,

the column was loaded with PBS (the mobile phase of the SEC column). Fifteen fractions of 500 μL volume each were collected. The first six fractions (3 mL) were discarded as void volume, whereas the rest of the nine fractions were analysed by NTA. EV-rich fractions were pooled together and used to test for EV-induced vascular inflammation.

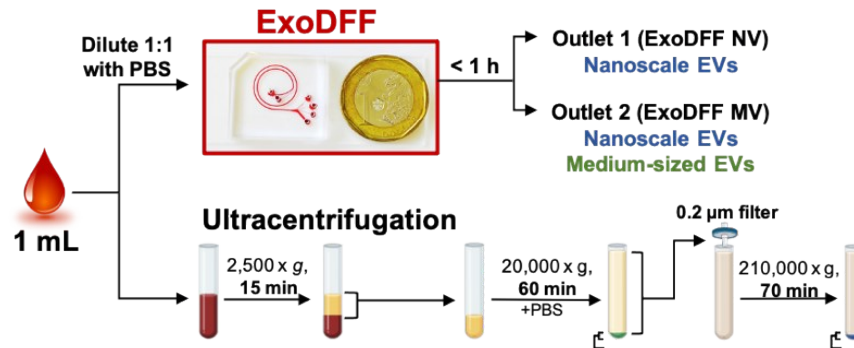


Figure S1. Workflow comparison between the single-step ExoDFF and conventional ultracentrifugation (UC) for isolation of circulating EVs from whole blood. Figure made with BioRender. Photograph shows the spiral device filled with red dye for visualization.

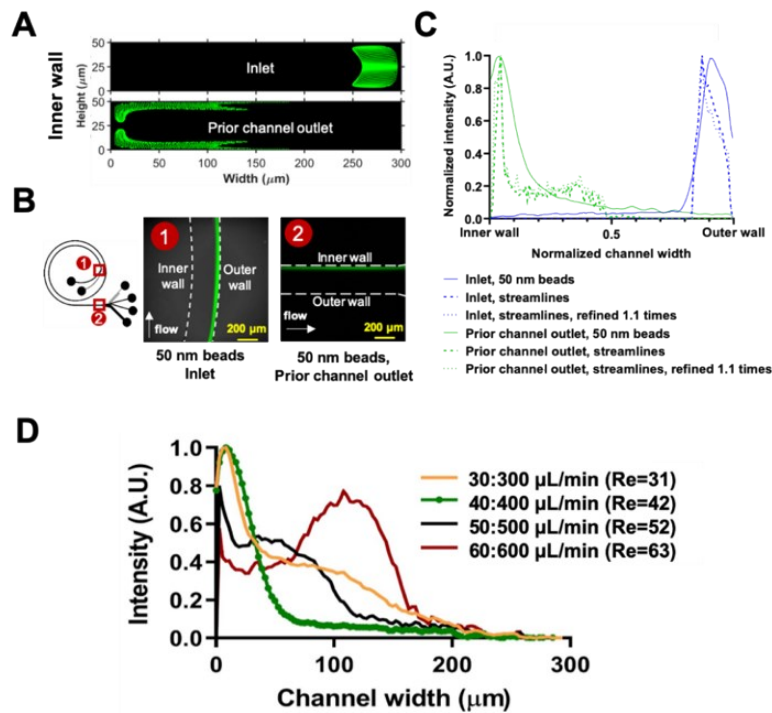


Figure S2. Experimental validation of CFD and flow rate optimization of ExoDFF. (A) Cross sectional views of fluid streamlines (mimicking nanoscale EVs) at different channel positions using CFD. (B) Top view fluorescent images of 50 nm beads at inlet and prior to channel outlet. (C) Comparison between average intensity linescans of 50 nm beads and streamlines at inlet and prior to channel outlet. Streamlines generated from two mesh sizes show similar intensity profile, indicating mesh independence of CFD solution. (D) Average intensity linescans of 50 nm beads at different Re indicating optimum flow rate at Re = 42.

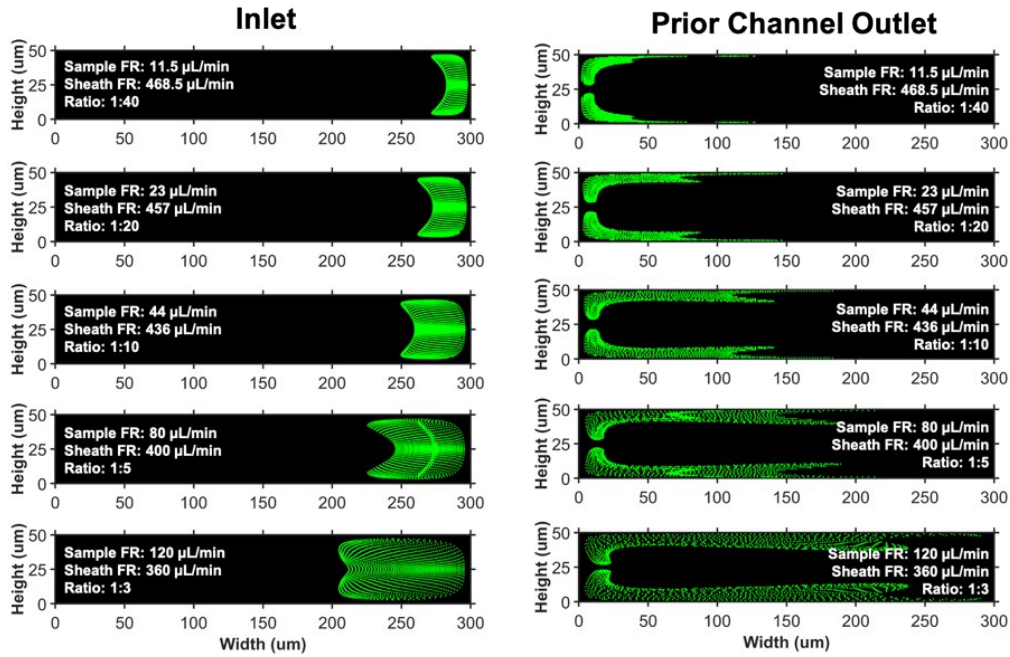


Figure S3. Cross sectional views of fluid streamlines (mimicking EVs) at device inlet and prior channel outlet at different sample to sheath flow rate (FR) ratio using CFD.

200 nm beads	Bead concentration (/mL)	Sample or Eluted volume (μL)	Final EV count	Separation efficiency
Inlet	5.10E+09	1000	5.1E+12	-
O1	4.60E+09	299	1.3754E+12	29%
O2	3.00E+09	757	2.27124E+12	47%
O3	7.37E+08	760	5.59813E+11	12%
O4	3.33E+07	17754	5.91803E+11	12%

Table S1. 200 nm beads concentration, sample elution volume and separation efficiency after ExoDFF isolation.

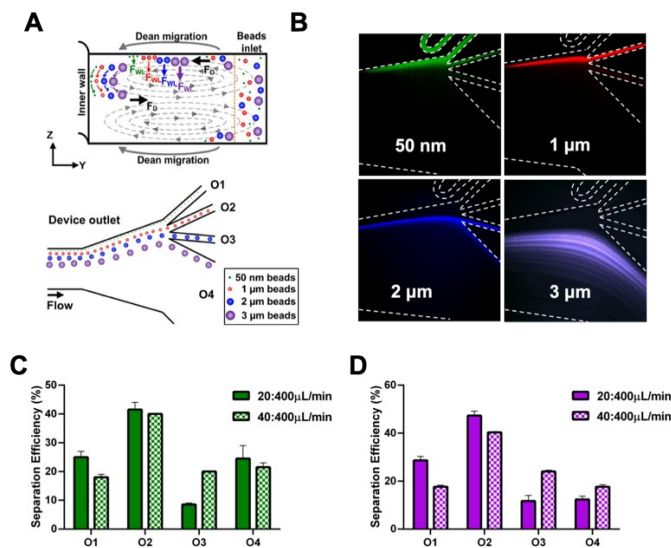


Figure S4. (A) Schematic illustration of ExoDFF sorting of different sized beads. (B) Corresponding fluorescent images illustrating flow streamlines of the different sized beads (50 nm to 2 μm) at optimized flow rate (Re 42). Beads separation efficiency of (A) 50 nm and (B) 200 nm beads at different sample:sheath flow rate ratio.

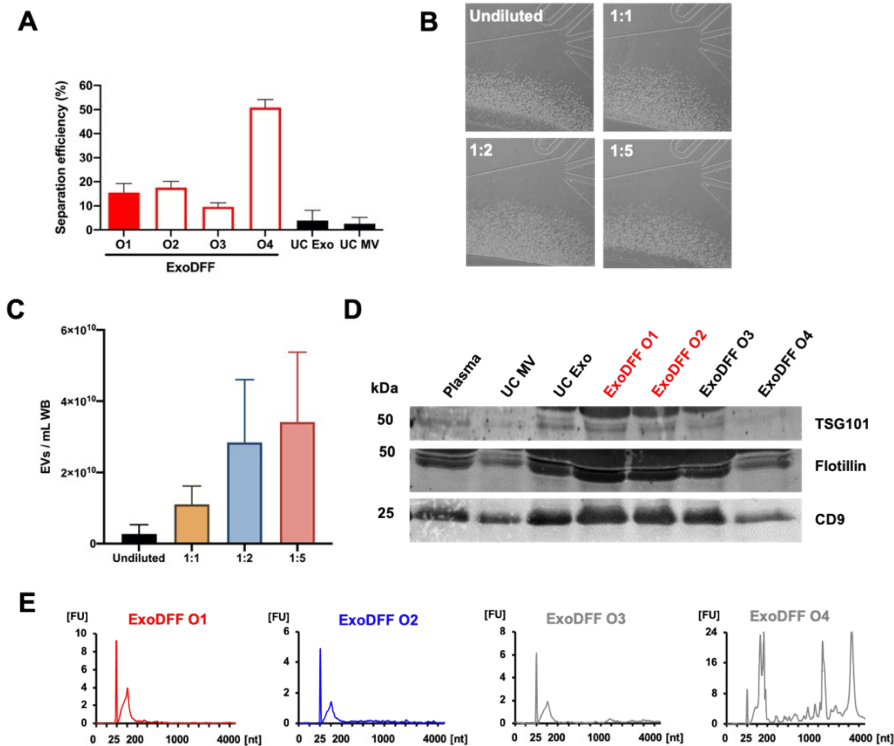


Figure S5. (A) EV separation efficiency from whole blood using ExoDFF (O1 – O4) and UC (n = 3, normalized to sample volume). (B) High speed images captured at the device outlet illustrating flow of RBCs at different blood dilutions. (C) EV yield from ExoDFF NV (O1) from undiluted and diluted (1:1, 1:2 and 1:5) blood samples (n=2). (D) Western blot detection of exosomal markers TSG101, flotillin and CD9 from UC and ExoDFF (O1 – O4) isolated EVs. All samples were loaded with equal volume (15 μ L) except plasma (0.5 μ L). (E) Bioanalyzer electropherograms showing the size distribution in nucleotides (nt) and fluorescence intensity (FU) of total RNA from ExoDFF outlets (O1 – O4).

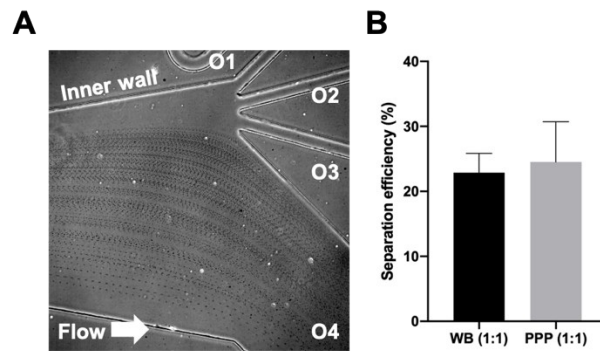


Figure S6: (A) Composite high speed image of platelet-poor plasma (PPP) processing using ExoDFF with platelets (~2-3 μ m appearing black dots) separating into outlet 3 (O3) and 4 (O4). (B) Separation efficiency comparison between diluted whole blood (1:1) and PPP (1:1) using ExoDFF (n=2).

Characteristics	Healthy (n = 5)	T2DM (n = 9)
Age* (Range)	35 (27 - 41)	53 (47 - 65)
HbA1c, %	5.340 (0.107)	7.278 (0.292)
Fasting glucose, mmol/L	5.160 (0.087)	7.667 (0.824)
BP Systolic, mmHg	104.500 (2.118)	125.000 (4.484)
CRP, mg/L	2.260 (0.822)	2.511 (0.686)
Total-C, mmol/L	4.580 (0.331)	3.756 (0.228)
HDL-C, mmol/L	1.240 (0.073)	1.122 (0.047)
LDL-C, mmol/L	3.020 (0.272)	2.1 (0.204)
Triglyceride, mmol/L	0.700 (0.071)	1.167 (0.121)

Average value shown with SEM in parentheses, unless otherwise indicated.

Table S2. Clinical characteristics of healthy (n = 5) and type 2 diabetic mellitus (T2DM) subjects (n = 9).

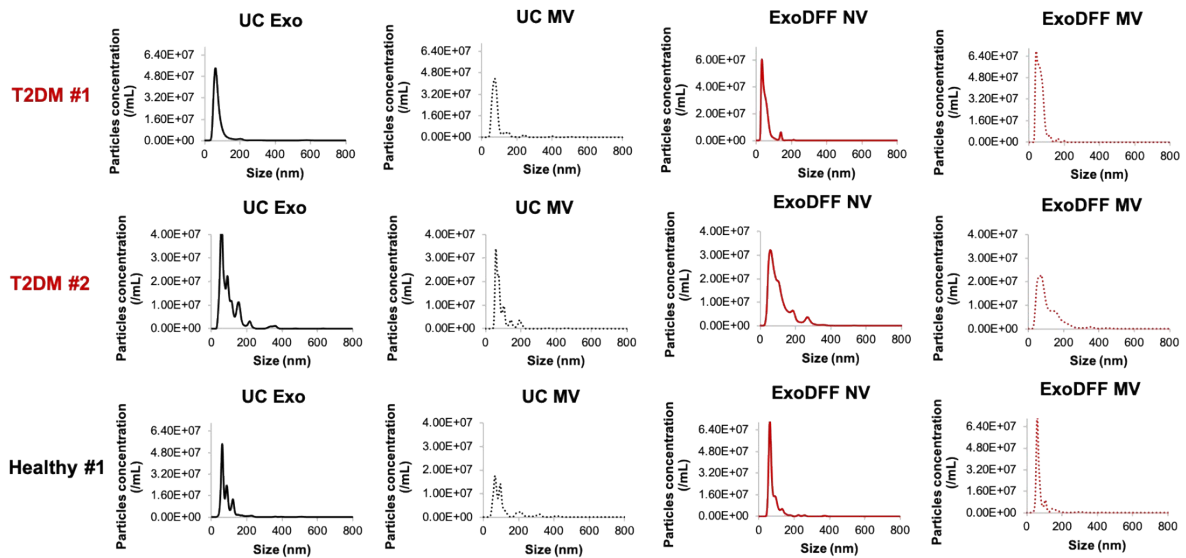


Figure S7. Representative NTA plots of EVs from healthy (n = 1) and T2DM (n = 2) subjects isolated using ultracentrifugation (UC) and ExoDFF.

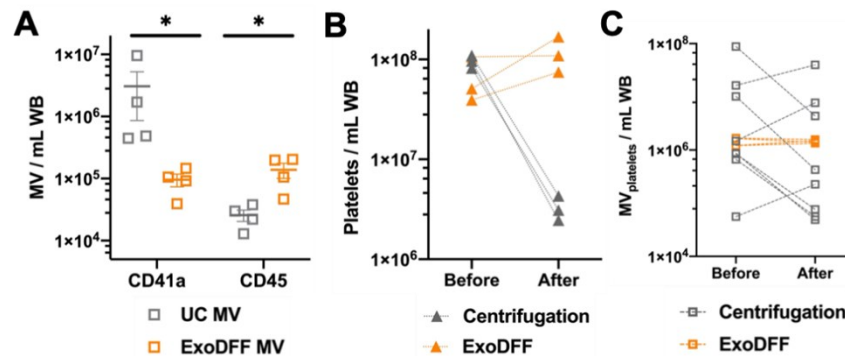


Figure S8. (A) Quantification of platelet-derived (CD41a+) and leukocyte-derived (CD45+) microvesicles isolated from UC MV and ExoDFF MV. (B) Significant platelet loss after high speed centrifugation (20,000 g, 45 min) in PRP samples as compared to ExoDFF (O3 – O4). (C) Significant variations in platelet-derived microvesicles in PPP samples after high speed centrifugation (20,000 g, 45 min) as compared to ExoDFF MV.

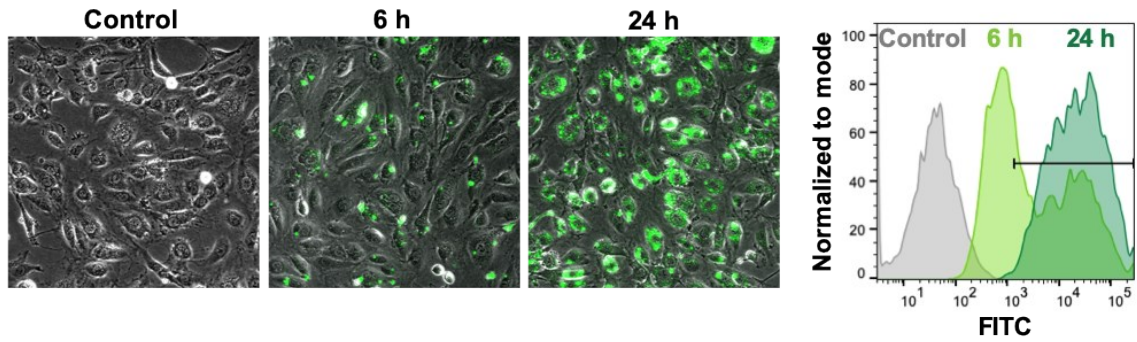


Figure S9. Representative bright-field and fluorescence overlaid images of HUVEC monolayer incubated without (control) and with fluorescence-labelled EVs (PKH67) after 6 and 24 h. Flow cytometry analysis of EVs uptake by HUVEC after 6 and 24 h.

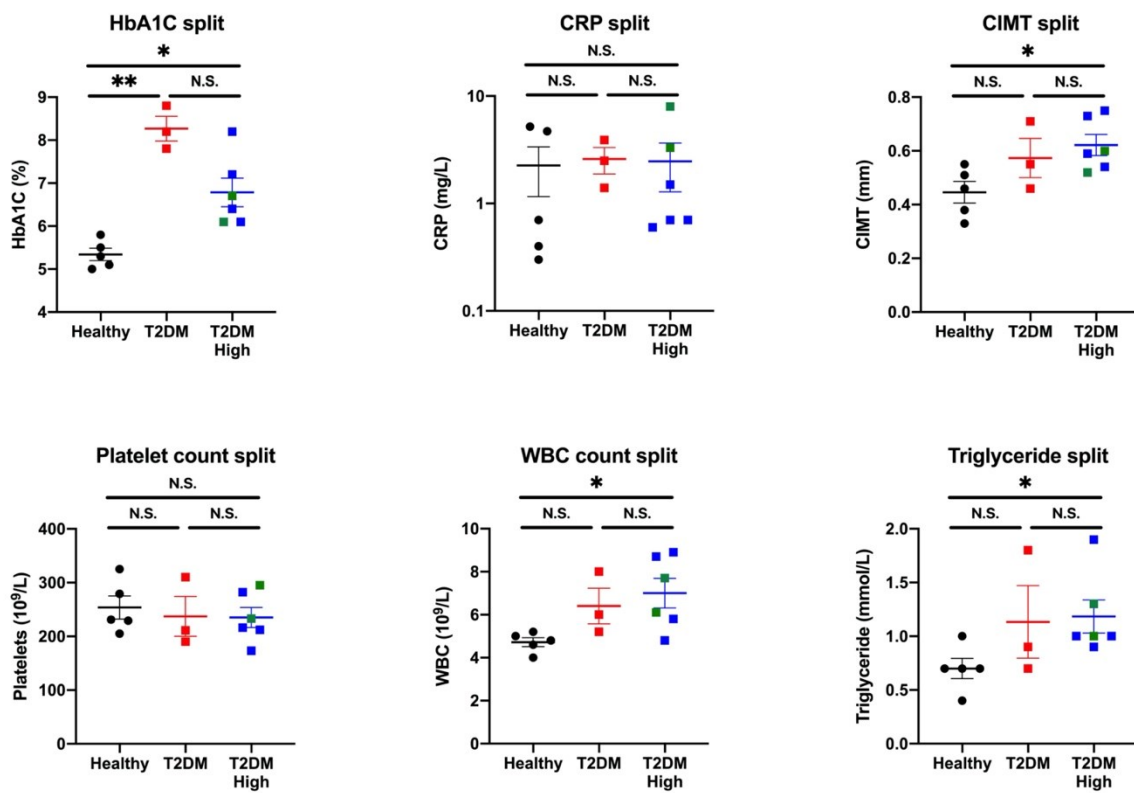


Figure S10. Clinical characteristics comparison of healthy (n = 5), T2DM (n = 3) and high risk T2DM (n = 6) subjects in terms of (A) HbA1C, (B) C-reactive proteins (CRP), (C) carotid intima-media thickness (CIMT), (D) platelet count, (E) white blood cell (WBC) count and (F) triglyceride levels.

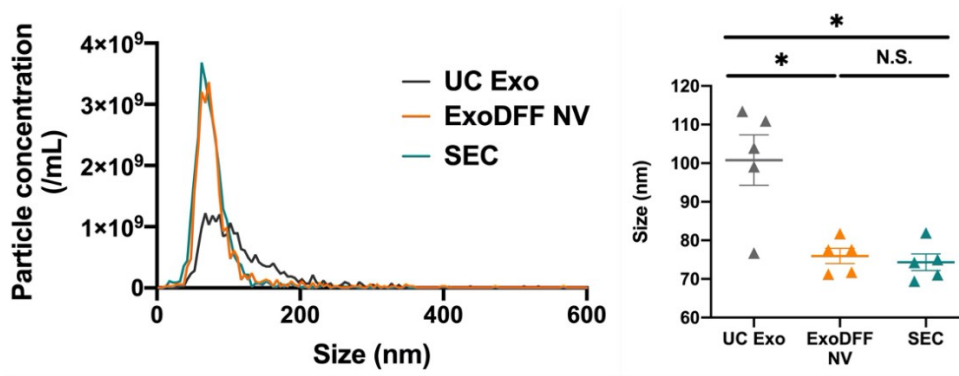


Figure S11. NTA size distribution profile (*left*) and EV size comparison (*right*, $n = 5$) of EVs isolated using ultracentrifugation (UC), ExoDFF and size exclusion chromatography (SEC).

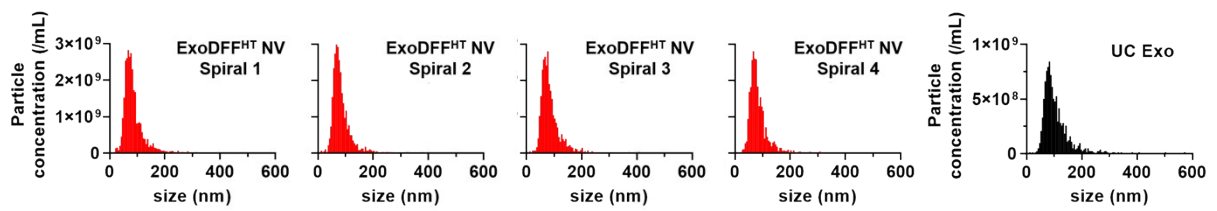
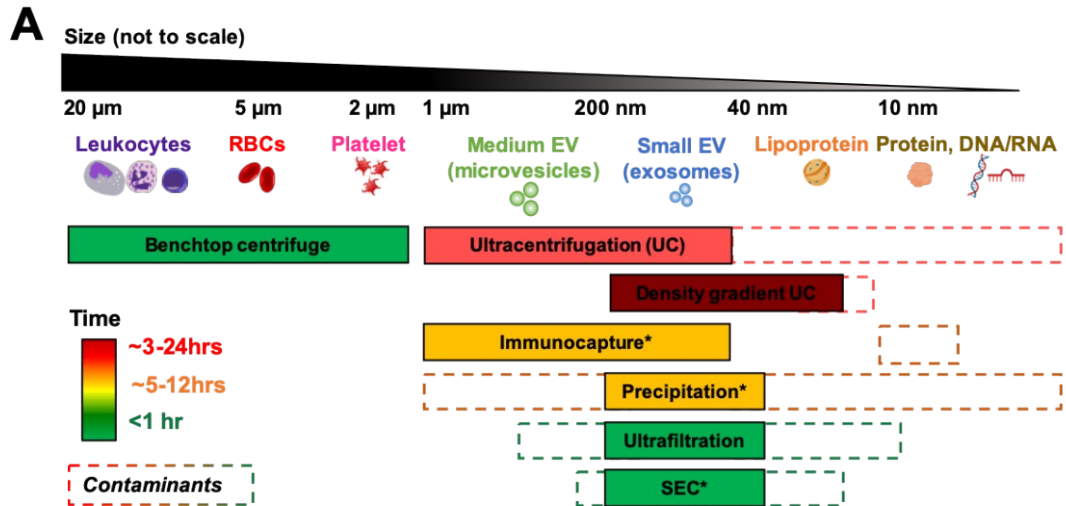


Figure S12. Representative NTA plots of EVs from each spiral of high throughput ExoDFF (ExoDFF^{HT} NV) and UC as control.



B

Methods	Differential Ultracentrifugation	Density Gradient Ultracentrifugation	Immunocapture	Precipitation	Ultrafiltration	Size Exclusion Chromatography
Principles	Sequential centrifugation to sediment cells, platelets, and EV at different rpm	Density-based EV fractionation in discontinuous density cushion or continuous density gradient	EV capture through binding with immobilized recognition elements including antibodies, aptamers	EV precipitation using water-excluding polymer which decreases EV solubility in medium	Size based separation through a porous membrane	Size dependent elution profile through a column packed with porous polymeric beads
Advantages	-Gold standard -Large capacity -Large dynamic range	-Low protein contamination -High purity -Large capacity	-High specificity -High purity	-Easy to use -High scalability	-Fast method -High scalability	-Low protein contamination -High reproducibility
Disadvantages	-Poor repeatability -High equipment cost -Low scalability	-Poor repeatability -High equipment cost -Low scalability	-High reagent cost -Low scalability -Low capacity	-Coprecipitation of protein and polymer precipitant	-Membrane clogging -Single size cutoff -Shearing of EV	-High dilution -Medium scalability
Contaminants	Lipoproteins, protein aggregates	Negligible	-Soluble proteins	MV, lipoproteins, protein aggregates	Lipoproteins	Lipoproteins
EV recovery (%)	~ 2 - 80	~10	~ 60 - 90	~ 90	~ 10 - 80	~ 40 - 90
Assay time (h)	~ 3 - 9	~ 16 - 90	~ 4 - 20	~ 0.3 - 12	~ 0.5	~ 0.3
Sample volume	mL - L	μL - mL	μL	μL - mL	μL - mL	μL - mL

Figure S13. Conventional methods for isolation of EVs. (A) Schematic overview and **(B)** table comparison on separation principles and various performance metrics for different methods.